Department of Physics and Astronomy
Heidelberg University

Bachelor Thesis in Physics
submitted by

Florian Schlötzer

born in Heilbronn (Germany)

2024

Temperature sensitivity study & verification of the MuPix11 fast differential data links for the Mu3e experiment

This Bachelor Thesis has been carried out by Florian Schlötzer at the
Physikalisches Institute in Heidelberg
under the supervision of
Prof. Dr. André Schöning

Abstract:
The aim of the Mu3e experiment is to observe the charged lepton flavor violating decay $\mu^+ \to e^+e^-e^+$ with a single event sensitivity of 1 in 2×10^{15}. This requires a detector with high rate capability, low material budget and precise spatial and time resulation, which is fulfilled by HV-MAPS. It combines sensor and readout-electronics in an ultra-thin chip. MuPix11 is a full scale $2\,\mathrm{x}\,2\,\mathrm{cm}^2$ HV-MAPS, used in the construction of the tracking detector of the Mu3e experiment. The sensors have to operate in a wide temperature range from 0 °C to 70 °C.
In this thesis the parameter space of the clocking and serialisation circuitries are investigated for its influence on the differential data link quality. An improvement of the signal quality can be achieved at the cost of a higher power consumption.
The stability and data integrity of the data links within an ambient temperature range from −20 °C to 80 °C is investigated for 70 µm and 50 µm thick MuPix11 sensors. Both can be operated within the specification defined by the Mu3e experiment. A linear decrease of the data signal amplitude with rising temperature is observed, which amounts to 18 % over the measured range. Nevertheless, a stable operation without transmission errors is feasible in all cases. The amplitude can be recovered by adjusting settings at the cost of up to 12 % increase in the total power consumption of the whole chip.

Zusammenfassung:
Das Ziel vom Mu3e Experiment ist den geladenen leptonfamilienzahlverletzenden Zerfall $\mu^+ \to e^+e^-e^+$ mit einer Einzel-Event-Sensibilität von 1 in 2×10^{15} zu beobachten. Dies erfordert einen Detektor mit hoher Ratefähigkeit, geringem Materialaufwand und präziser räumlicher und zeitlicher Auflösung, was durch HV-MAPS erfüllt wird. MuPix11 ist ein vollskaliger $2\,\mathrm{x}\,2\,\mathrm{cm}^2$ HV-MAPS, das beim Bau des Spurdetektors des Mu3e-Experiments verwendet wird. Die Sensoren müssen in einem weiten Temperaturbereich von 0 °C bis 70 °C betrieben werden.
In dieser Arbeit wird der Parameterraum der Takt- und Serialisierungsschaltungen auf ihren Einfluss auf die Qualität des differentiellen Datenlinks untersucht. Eine Verbesserung der Signalqualität kann auf Kosten eines höheren Stromverbrauchs erreicht werden.
Die Stabilität und Datenintegrität der Datenlinks innerhalb eines Umgebungstemperaturbereichs von −20 °C bis 80 °C wird für 70 µm und 50 µm dicke MuPix11-Sensoren untersucht. Beide können innerhalb der vom Mu3e-Experiment definierten Spezifikationen betrieben werden. Es wird ein linearer Abfall der Datensignal-Amplitude mit steigender Temperatur beobachtet, der über den gemessenen Bereich 18 % beträgt. Dennoch ist ein stabiler Betrieb ohne Übertragungsfehler in allen Fällen möglich. Die Amplitude kann durch Einstellungen wiederhergestellt werden, was jedoch mit einem bis zu 12 % höheren Stromverbrauch des gesamten Chips verbunden ist.

Contents

Part I.
Introduction & theory

1. Introduction

Over the years the Standard Model of Particle Physics (SM) proved to be an excellent theory to describe the components of the visible matter as well as the interactions holding them together. One of the biggest successes was the prediction of the Higgs boson, which was verified 2012 at the LHC. Still, some observed phenomena can not be explained by the SM. Therefore, efforts are made to find inconsistencies to expand the theory to physics beyond the SM.
The observation of neutrino oscillations indicates that, contrary to previous assumption, neutrinos have a mass. With this expansion the construction of a Feynman diagram of the charged lepton flavor violating decay $\mu^+ \to e^+e^-e^+$ is possible. In the SM, this decay is suppressed to a branching ratio below 10^{-54}, making it not observable within a reasonable experimental timescale. The observation of this decay would be an indication of new physics beyond the SM. The Mu3e experiment aims to find or exclude the decay for a branching ratio above 10^{-16} at a 90 % confidence level. To perform the experiment in the reasonable time, a high rate detector is needed. The MuPix11 sensor utilizes High-Voltage Monolithic Active Pixel Sensor (HV-MAPS) technology. This silicon pixel sensor can be thinned down to 50 µm and is able to handle high rates with precise time and spatial resolution.
This sensor needs to perform in the temperature range from 0 °C to 70 °C in the experiment, which will influence the data link signals. To investigate the performance at different temperatures, the signal quality of the data links of MuPix11 sensors are observed via eye diagrams in this thesis. The important parameters are the signal amplitude, the eye width, related to the signal noise, the eye width, related to the signal jitter and the Q-factor, a typical measure for the signal quality.
First, the setting of the digital components, controlled through digital to analog converters (DACs), are investigated. By observing changes in the eye diagram the influence of the different electronic components on the signal are investigated. Therefore, the eye parameter are plotted as a function of the values for the different DACs, as long as no transmission errors occur. With this knowledge the signal in the data links can be optimized.
Afterwards a 70 µm and a 50 µm MuPix11 sensor are exposed in a climate-controlled environment to ambient temperatures ranging from −20 °C to 80 °C, the expected range in the Mu3e experiment. For both thicknesses the eye parameter are plotted as a function of the ambient temperature in 10 °C steps. In addition to the eye diagrams, currents in the sensor diodes

and supply voltages on the sensor are observed as a function of the ambient temperature to guarantee a safe operation within the specification.
For the decrease of the signal quality with increasing temperature, the knowledge of the influence of the DACs are used to recover the signal for high temperatures.
In order to generalize the temperature dependence, the other data links as well as different mirroring modes and multiplexing for link 4 are investigated qualitatively.

2. The Standard Model and beyond

2.1. The Standard Model of Particle Physics

In the current state, the Standard Model of Particle Physics (SM) is one of the most successful theory in modern physics. The SM is a gauge theory to understand the elementary particles and their interactions. The elementary spin $\frac{1}{2}$ particles (fermions) are divided in three families, with each family consisting of quarks (fractional charge) and leptons (integer charge). There are six flavor of quarks and six flavors of leptons. The lepton flavors can be grouped in families, the electronic leptons, the muonic leptons and the tauonic leptons. Each particle also has an antiparticle that differs in its opposite charge. The three of the four fundamental interactions are integrated into the SM - the electromagnetic, the strong and the weak force. The carriers of these fundamental interactions are the four (gauge) bosons. The scalar boson, the Higgs boson, explains how fundamental particles acquire mass. The different masses, charges and spins of fermions and bosons are summarized in Figure 1.
Despite the success of the theory, there are still some unexplained questions in the physics community. The SM can not answer, for example why the fermions are divided into exactly three families or how does the fourth fundamental interaction, the gravitational force, fit into the SM.

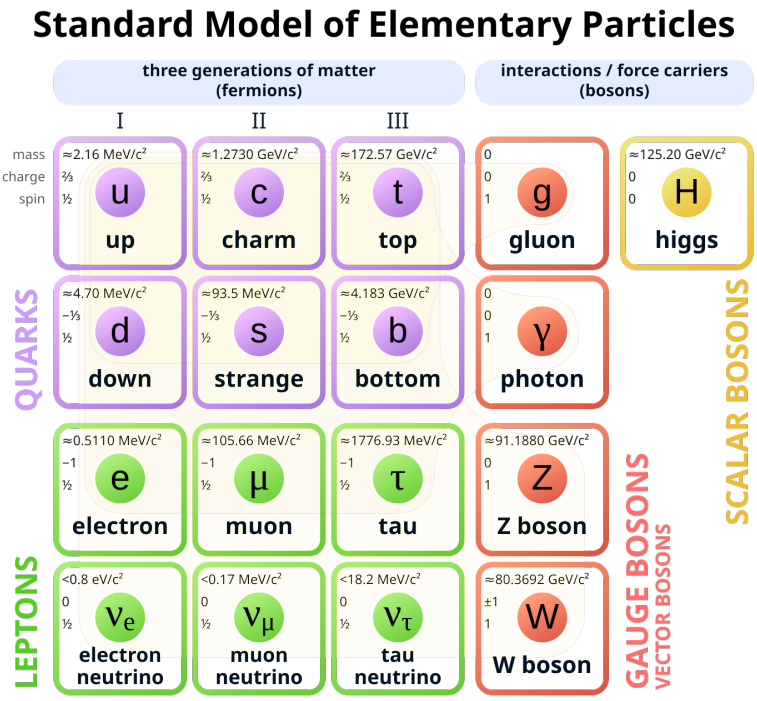

Figure 1: Standard Model of Elementary Particles [1].

2.2. Charged Lepton Flavor Violation

The SM does not give an explanation for particle interactions violating the lepton flavor conservation, instead lepton flavor is a conserved quantity. But the detection of neutrino oscillations indicates charged leptons must experience lepton flavor violating interactions [2]. Charged lepton flavor violations (CLFV) are not observed directly, yet. Efforts to include massive neutrinos in the SM to explain neutrino oscillation allows CLFV, but with branching ratios many orders of magnitude below the resolution possible in current and planned experiments. For example, the branching ratio of the decays $\mu^+ \to e^+ \gamma$, $\mu^+ \to e^+e^-e^+$ or $\tau^\pm \to e^\pm \gamma$ is $\lesssim 10^{-53}$ [3, 4]. Observing one of these highly suppressed decays in an experiment would therefore indicate existence of new physics beyond the SM. Experiments like Belle [5] or SINDRUM [6] try to experimentally verify these limits by increasingly upgrading their measurement accuracy and determine upper limits for the branching ratio of CLFV processes. An overview of the current (25 May 2022) experimental upper limits on the branching ratios of CLFV processes for muons is given in Table 1. The complete list for CLFV muon, tau, meson (π , J/ψ , B, K) and boson (Z^0, h) processes are found in [7] (Table 3). One planned experiment to further measure the upper limit of the $\mu^+ \to e^+e^-e^+$ decay is the Mu3e experiment.

Process	Experiment	Exp. Limit	Confidence Level
$\mu^+ \to e^+ \gamma$	MEG	4.2×10^{-13}	90%
$\mu^+ \to e^+e^-e^+$	SINDRUM	1.0×10^{-12}	90%
$\mu^-\mathrm{N} \to e^-\mathrm{N}$	SINDRUM-II	6.1×10^{-13}	90%
$\mu^-\mathrm{N} \to e^+\mathrm{N}'$	SINDRUM-II	5.7×10^{-13}	90%

Table 1: Current experimental upper limits of the branching ratio of CLFV processes for muons adopted from [7].

3. The Mu3e experiment

The goal of the Mu3e experiment is to detect the CLFV decay $\mu^+ \to e^+e^-e^+$ for a branching ratio as low as 10^{-16}, or to excluded the decay for larger branching ratios at the 90 % confidence level. To achieve these goals within a reasonable measurement time of one year, a muon stopping rate of 2×10^9 Hz is required.
The experiment will take place at the πE5 beam line at PSI, providing muon rates up to 10^8 Hz, the currently highest possible in the world. In 2025, the beam line will be upgraded to achieve the higher muon intensities required to reach the target limit. To test the developed technology and setup, and to set a first limit of the branching ratio, a first phase of data taking is planned at πE5 before the shutdown. With a planned muon stopping rate of 10^8 Hz and an aimed single event sensitivity of 2×10^{-15} on the branching ratio over 2.5×10^{15} muons need to be stopped, corresponding to a experiment run time of 2.5×10^7 s (290 days).

3.1. $\mu^+ \to e^+e^-e^+$ signal and background

With the expansion of including neutrino oscillation in the SM the decay $\mu^+ \to e^+e^-e^+$ is possible, but has a branching ratio below 10^{-54} [8]. In an experiment other muon decays with much higher probability will occur and produce an irreducible background.
The decay products are emitted from the same location at the same time from a (anti)muon at rest. Due to momentum and energy conservation the vectorial sum of momentum of the decay particles is:

$$|\vec{p}_{total}| = |\sum \vec{p}_{decay}| = 0. \tag{1}$$

Since the initial momentum vanishes, the inertial mass becomes

$$m_{inv} = \sum E_{decay} = m_{muon}. \tag{2}$$

For the $\mu^+ \to e^+e^-e^+$ decay the two positrons and one electron need to fulfill Equation 1 and Equation 2. Therefore the particles need to be tracked and their momentum needs to be measured.
The background in the Mu3e experiment consist of muon decays mimicking the decay products of two positron and one electron. The largest contribution to the background is the accidental combination of two positron tracks from locally close muon decays, where one electron is ejected from the target via Bhabha scattering [4]. Scintillating fibres and tiles are used to increase the precision of the timing information and distinguish the CLFV decay from the accidental background.

Another example of the background is the decay $\mu^+ \to e^+e^-e^+ \nu_e \bar{\nu}_\mu$ with a branching ratio of 3.4×10^{-5} [6], which conserves lepton flavor and is allowed in the SM. Since the neutrinos will not be detected, the decay products observed are the same as for $\mu^+ \to e^+e^-e^+$. But because of the two extra neutrinos, the sum of their energy is smaller than muon rest mass. To distinguish the $\mu^+ \to e^+e^-e^+$ decay from this background process the average three-particle mass resolution must be better than 1.0 MeV [4]. Overall a the spatial and time resolution of the detector must be very precise to distinguish the CLFV decay from the background.

3.2. Experimental setup

The setup of phase I of the Mu3e experiment is schematically shown in Figure 2. The muon beam at PSI is stopped on a hollow double-cone target made of aluminised Mylar foil. The decay products then pass through multiple pixel sensor layers arranged in cylindrical form around the stopping target. The two inner layers (layer 1 and 2) and the two outer layers (layer 3 and 4) are used to track the trajectory of the particles. The geometry of the layers and their number of sensors are summarized in Table 2. The recurl layers, used to increase the number of reentering particles, have two sensor layers identical in geometry to the outer layers in the central tracker. By the outer and recurl layers the scintillating fibres and layers are located, providing precise timing information to suppress background. To allow to measure the momentum of the charged particle the whole setup is put into a superconducting solenoid magnet providing a homogeneous magnetic field of B = 1 T.

layer	minimum radius from target [mm]	instrumented length [mm]	number of sensors
1	23.3	124.7	48
2	29.8	124.7	60
3	73.9	351.9	408
4	86.3	372.6	504

Table 2: Geometry parameter of the different layer [4].

The main limiting factor of the momentum resolution in the detector will be Coulomb scattering. Therefore, the material budget of the sensor needs to be minimized, while still being able to handle high particle rates. The requirements for the Mu3e sensor is summarized in Table 3. With the High-Voltage Monolithic Active Pixel Sensor (HV-MAPS) technology such an ultra-thin silicon pixel sensor, the MuPix11, was developed (see subsection 6.1). The radiation length per layer including the electronic services for such a sensor is approximately $X/X_0 = 0.115\,\%$.

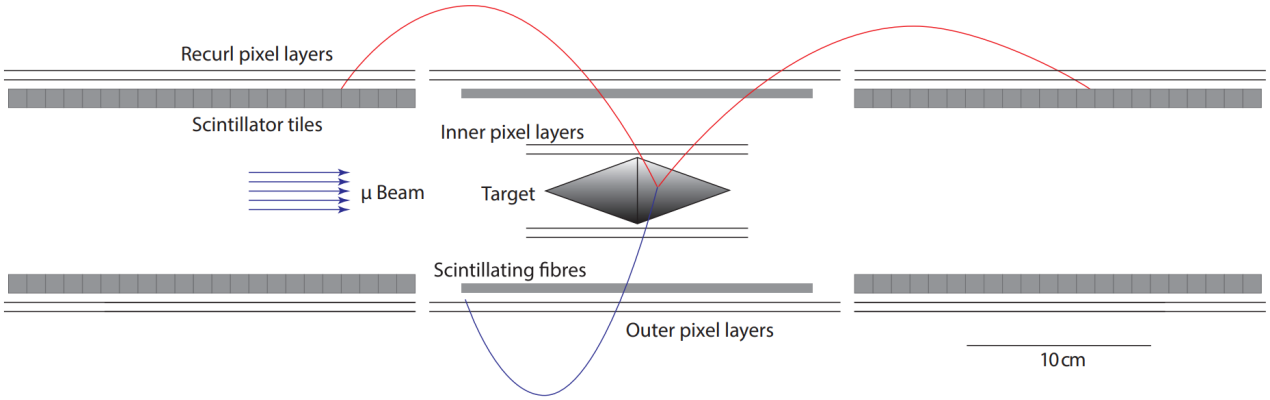

(a)

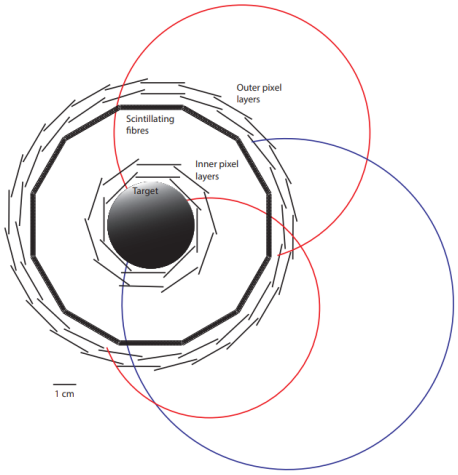

(b)

Figure 2: Schematic view of the Mu3e experiment in phase I cut (a) along the beam axis and (b) transverse to the beam axis [4].

sensor dimensions $[mm^2]$	≤ 21
sensor size (active) $[mm^2]$	$\approx 20 \times 20$
thickness [µm]	≤ 50
spacial resolution [µm]	≤ 30
time resolution [ns]	≤ 20
hit efficiency [%]	≥ 99
number of LVDS links	3+1
bandwidth per link [Gbit/s]	≥ 1.25
power density of sensors $[\mathrm{mW}/cm^2]$	≤ 350
operation temperature range [°C]	0 to 70

Table 3: Requirements for the Mu3e pixel sensors [4].

3.3. Detector cooling

While operating the sensors, a heat dissipation of around $350\,\mathrm{mW/cm^2}$ is expected. Because of the tight geometry of the layers, the sensors would heat up to more than 140 °C without active cooling [9]. But the temperature needs to be kept safely below 70 °C, the glasstransition temperature of the adhesives used for construction. To minimize Coulomb scattering, the cooling material budget must be kept as low as possible. Therefore the tracking pixel sensors are cooled by gaseous helium. The initial temperature of the helium is $\gtrsim -20\,°\mathrm{C}$ [10] and flows parallel to the layer. While it flows along the layers, the temperature of the helium increases and its ability to cool the sensors get worse. A simulation of the temperature dependence of the pixel layers is shown in Figure 3. The initial temperature of the helium in the simulation is 0 °C, the originally planned temperature for Mu3e. It shows, that the sensors will be exposed to a wide range of temperature. The influence of the temperature on the data links is described in section 10.

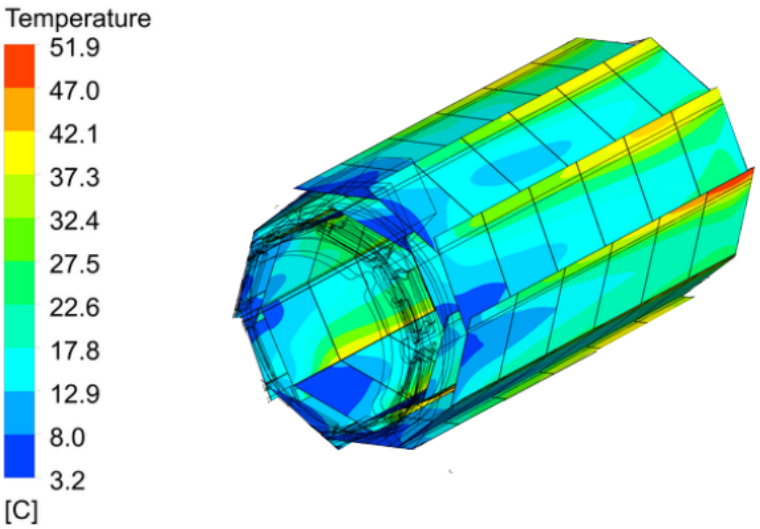

Figure 3: Simulated temperature distribution of the silicon layers for a power dissipation of $400\,\mathrm{mW/cm^2}$ and initial helium temperature of 0 °C [4].

4. Particle Interaction with Matter

In all particle interactions energy from one particle gets transferred to another one via the electromagnetic, the strong or the weak force. The type of particle determines which interaction is possible: charged particle and photon interact electromagnetic, hadrons interact strong and neutrinos interact weak. The medium as well as the characteristics of the incident particle determines the amount of energy transmitted.
The most common detectors use electromagnetic interaction to measure particles. The energy loss of photons and charged particles can happen via different effects addressed in this chapter.

4.1. Photons

In general, three effects describe the interactions between photons and matter:

Photoelectric effect: The photon completely transmit its energy to an atom, which then emits an electron. The resulting vacancy in one of the atomic shells is filled by an electron of the higher shells, emitting a photon again.

Compton scattering: The photon performs elastic scattering on an free or quasi-free electron. In Compton scattering, quasi-free electrons are shell electrons of atoms with binding energies much lower than the photon energy. The energy loss results in a wavelength shift of the photon.

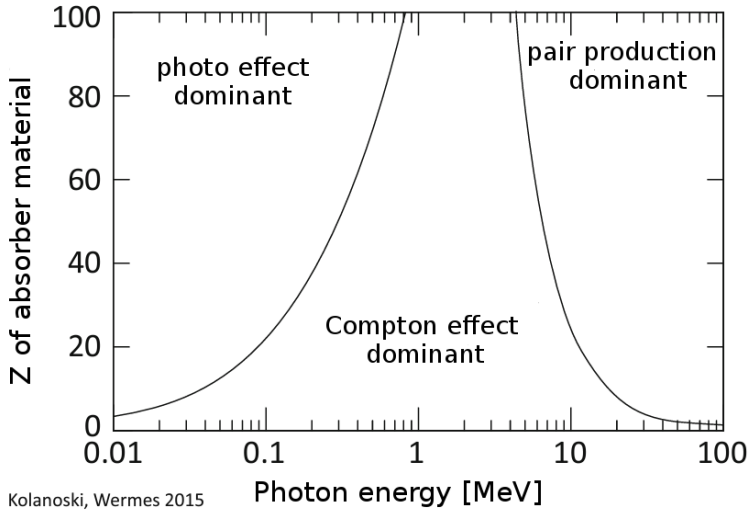

Figure 4: Domains of the different dominant processes for photons [11].

Pair production: In the presence of a Coulomb field of a charged particle, the photon can transform into an electron-positron pair.

Which effect is dominant depends on the number of protons Z of the interaction material and the photon energy (see Figure 4) [11].

4.2. Charged particles

Charged particles can experience a diverse range of energy transmission effects, influenced by the properties of both the incident particle and the interacting medium. Some of these effects are described by:

Bethe-Bloch formula For heavy charged particles their energy is transmitted to the electrons of the material atoms by excitation or ionization. In this case "heavy" corresponds to particle with rest mass much higher than electrons [12]. The Bethe-Bloch formula describes the energy loss per path length and reads as [13]:

$$-\left\langle \frac{dE}{dx} \right\rangle = \frac{4\pi n z^2}{m_e c^2 \beta^2} \cdot \left(\frac{e^2}{4\pi\epsilon_0} \right)^2 \cdot \left[\log\Big(\frac{2 m_e c^2 \beta^2}{I \cdot (1-\beta^2)} \Big) - \beta^2 - \frac{\delta(\beta\gamma)}{2} \right]. \tag{3}$$

with the the electron density n, the charge number z, the electron mass m_e, the speed of light c, the velocity in speed of light β, the vacuum permittivity ϵ_0, the mean excitation energy I and the density-effect correction $\delta(\beta\gamma)$. The formula is plotted as a function of $\beta\gamma$ in Figure 5 for different interaction materials. For all materials the global minimum is by $\beta\gamma \sim 3$. Particles with this energy are called minimum ionizing particles.

Bremsstrahlung For highly relativistic charged particles the energy loss occurs by emitting a photon. This radiation is called Bremsstrahlung. Due to their small masses, electrons and positrons become relativistic at relatively small energies [12].

Multiple Coulomb scattering Charged particles scatter in the Coulomb field of atomic nuclei. For incident particles passing through matter multiple of these Coulomb scattering happen, resulting into an overall deflection angle θ_{plane} (see Figure 6). A Gaussian approximation can be used to describe the RMS width of the angular distribution as [14]:

$$\theta_{plane}^{RMS} = \frac{13.6\,\mathrm{MeV}}{\beta c p} z \sqrt{\frac{x}{X_0}} \left[1 + 0.038 \cdot \ln\Big(\frac{x z^2}{X_0 \beta^2} \Big) \right], \tag{4}$$

with the momentum p, the velocity in speed of light β, the speed of light c, the charge

number z and the relative radiation length x/X_0.

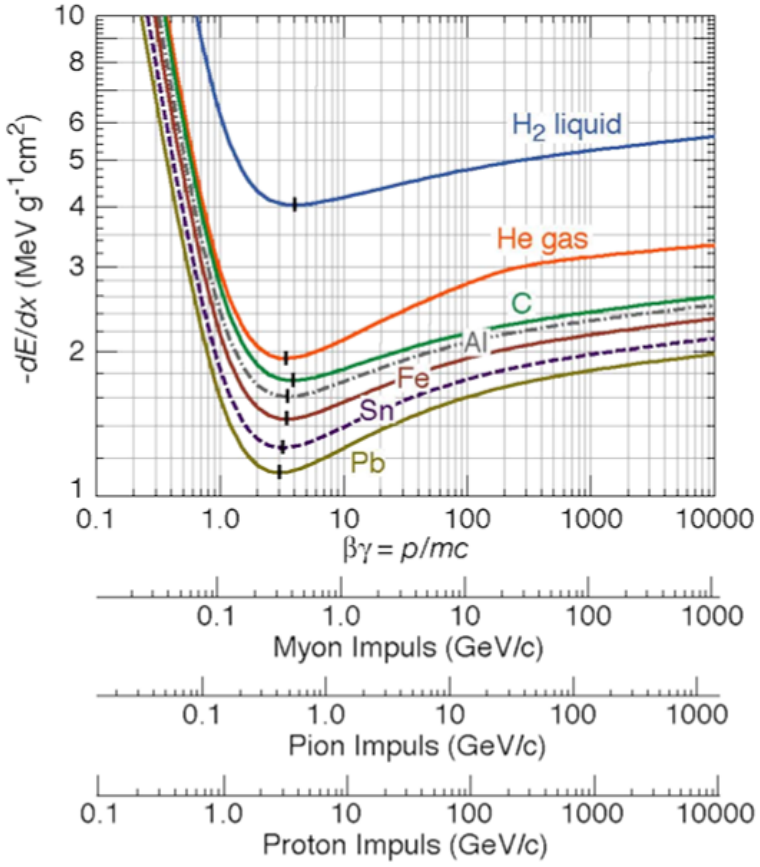

Figure 5: Bethe-Bloch formula for a heavy charged particle in different interaction materials [14].

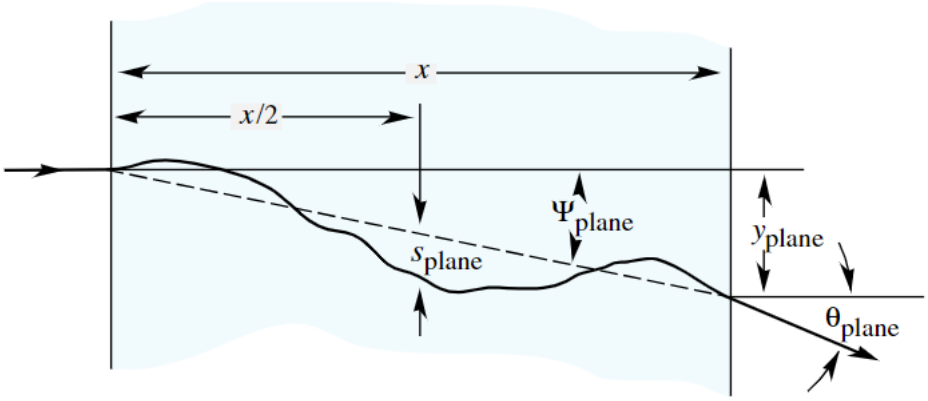

Figure 6: Sketch of the track of a charged particle experiencing multiple Coulomb scattering in matter [14].

5. Semiconductor Physics

Semiconductor are used in every modern electrical device, in everyday live as well as in physic experiments. Their use in transistors and in detectors make them of high value and interest. In this section the fundamental working principles of semiconductors, the basic components and how they are used to detect particles are described.

5.1. Energy gap

In solid-state physics the conductivity of a solid is determined by the band gap between the valence band and the conduction band. The valence band is the highest energy range where the electrons are bound in the solid, while the conduction band marks the lowest energy range of free-moving electrons. The band gap is the energy gap between the two bands. In pure materials no electron state can exist in the band gap due to quantization of energy. Therefore to be conductive the electrons must be able to overcome this gap by adding thermal energy to the system. At temperature $T = 0\,K$ the Fermi level is highest energy state electrons can occupy. In the case of metals, the two band overlap and electrons can always move freely, making metals good conductors. In the case of insulators, the energy gap is too large for electrons to overcome. Semiconductors also have a band gap, but much smaller and near the Fermi level (see Figure 7). In this situation the valence band is fully occupied and the conduction band is completely empty. For temperatures above $0\,K$ the electrons can overcome small gaps like in semiconductors due to thermal excitation. Every electron reaching the conduction band leaves a positive charged hole in the valence band, also contributing to the conduction of the semiconductor. The holes are free charge carrier with similar properties as electrons, but with opposite charge and different mobility [11, 16].

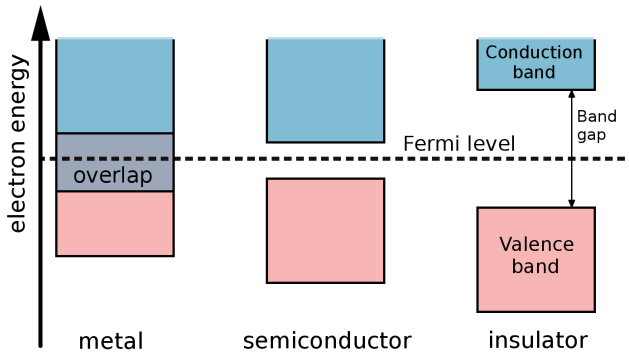

Figure 7: Comparison of band gap between metal, semiconductor and insulator. Adapted from [15].

5.2. Intrinsic semiconductors

In pure, intrinsic semiconductors the intrinsic charge carrier density n_i read like

$$n_i = 2 \cdot (m_e^* \cdot m_h^*)^{3/4} \cdot \left(\frac{k_B T}{2\pi\hbar^2} \right)^{3/2} \cdot e^{-E_g/(2k_B T)} \tag{5}$$

with the effective electron and hole mass m_e^* and m_h^*, the Boltzmann constant k_B, temperature T, the reduced Planck constant $\hbar$ and the band gap energy E_g [16]. An intrinsic silicon semiconductor has for $T = 300\,\mathrm{K}$ and the band gap of $E_{g,Si} = 1.11\,\mathrm{eV}$ an intrinsic charge carrier density of $n_{i,Si} \approx 10^{16}\,\mathrm{m}^{-3}$. Compared to the metallic conductor copper with a charge carrier density of $n_{Cu} = 8.47 \times 10^{28}\,\mathrm{m}^{-3}$ [17] the intrinsic semiconductor has is a bad conductor for all practical applications.

5.3. Extrinsic semiconductors

To increase the charge carrier density, a method called doping is used. Here, impurities are added to the atomic lattice intentionally. Explained in the case of silicon, a four-valent element, doping is done by adding three-valent atoms, called acceptors, or with five-valet atoms, called donors. The replacing of the origin atoms with dopant atoms add extra holes or electrons in the structure (see Figure 8). By introducing impurities into the crystal, additional energy states within the energy gap are formed. The extra energy states created by doping allows the transition of electrons and holes between the valence band and the conduction band with

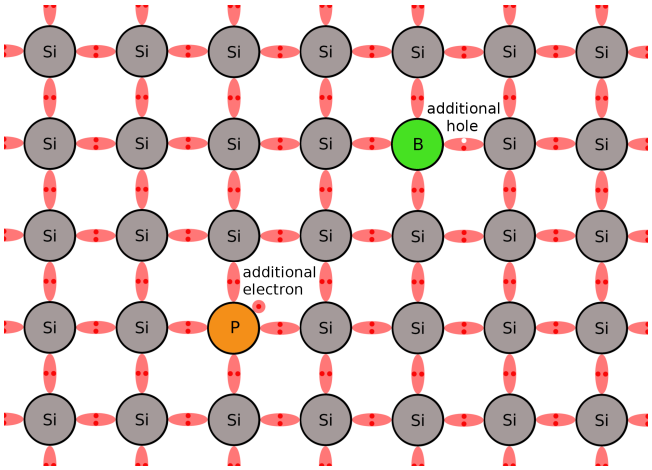

Figure 8: Covalent bonding of silicon atoms exemplary with a bor and a phosphor atom as impurities.

less energy. In the case of donor atoms, the energy states lie just below the conduction band, making it easier for electrons to move into the conduction band. For acceptor atoms, the energy states lie just above the valence band, allowing electrons to move from the valence band into these states, leaving behind extra holes. In n-doped semiconductors the electrons are the major carrier and the holes are the minor carrier. For p-doped semiconductor the names are reversed. The charge carrier density n_i of an extrinsic semiconductor follows also Equation 6[11].

5.4. Diodes

If an p-doped and an n-doped semiconductor are brought into physical contact, an p-n junction is created. Due to the different density of charge carrier on both sides, free electrons and holes drift to the contact surface. At the contact surface the free electrons and holes of both sides diffuse and recombine, creating an insulating so called depletion region, where no free charge carrier are left. In this region the doping atoms remain as ions, creating an electric field. By applying a voltage on both sides of the junction, the size of the depletion region can be adjusted. In forward bias (negative pole at n-doped, positive pole at p-doped) the depletion zone shrinks due to increase in major carriers in both semiconductor, while in reverse bias (negative pole at p-doped, positive pole at n-doped) the depletion zone grows due to the removable of major carriers (Figure 9). In forward bias for high enough external voltages (for Si >0.7 V) the system behaves as a conductor [16, 18]. In reverse bias the system behaves as a insulator, but still a leakage current flows. Such a system is called a semiconductor diode. The leakage current depends on the charge carrier density n_i and the charge carrier generation lifetime $\tau_g \sim T^{-1/2}$

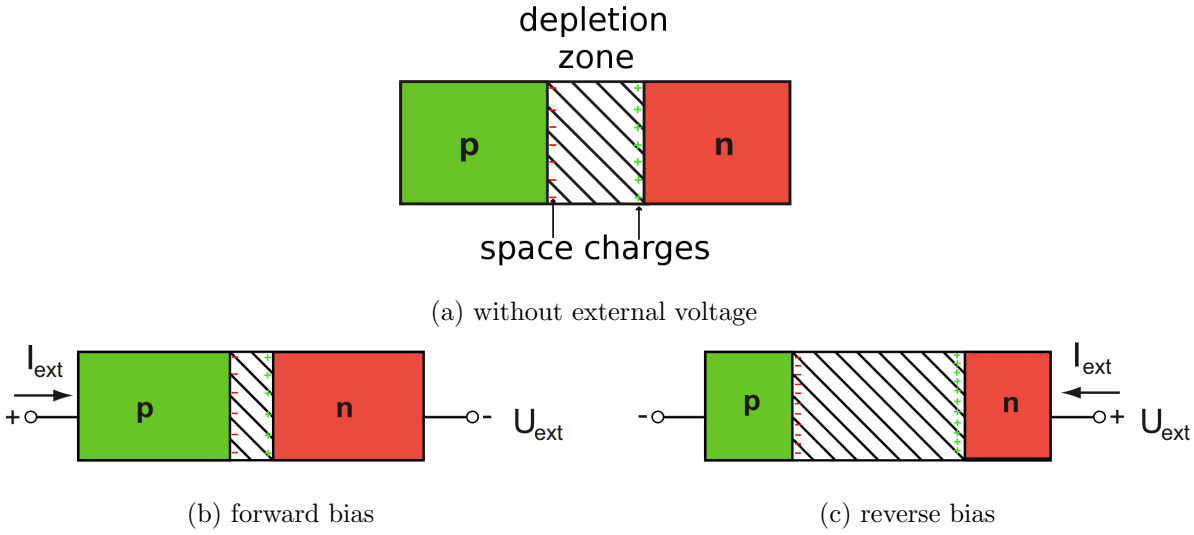

(a) without external voltage

(b) forward bias

(c) reverse bias

Figure 9: Diode without and with external voltage: (a) without external voltage, (b) in forward bias and (c) in reverse bias. Adapted from [11].

and reads as [19]:

$$I_L \sim \frac{n_i}{\tau_g} \sim T^2 e^{-\frac{E_a}{2kT}} \tag{6}$$

with the effective energy E_a.

5.5. MOSFET

The "Metal–Oxide–Semiconductor Field-Effect Transistor" (MOSFET) is a voltage controlled transistor. Due to their small form factor and low power consumption, these transistors are most common used. The mode of operation is described exemplarily below based on the n-channel MOS (NMOS) (see Figure 10 left). In a weakly p-doped silicon substrate, two heavily n-doped implants form the drain and source areas of the transistor. The gate electrode is located between the n-doped areas, isolated from the surface by a thin oxid layer (normally SiO_2). By applying a positive voltage at the gate, the electric field under the electrode changes. The valence and conduction band are bent at the surface until at some point the conduction band is below the Fermi energy. This creates a conductive channel, the inversion layer. With increasing gate voltage applied the voltage between source and drain has an ohmic, a saturated and then a pinch-off mode.
"Complementary Metal-Oxide-Semiconductor" (CMOS) transistors are NMOS and p-channel MOS (PMOS) transistors on the same substrate (see Figure 10). A significant advantage of CMOS technology is that current in the circuits flows only when the transistors change states from ON to OFF or vice versa.. Otherwise, only leakage current is present, allowing an energy efficient operation [11, 20].

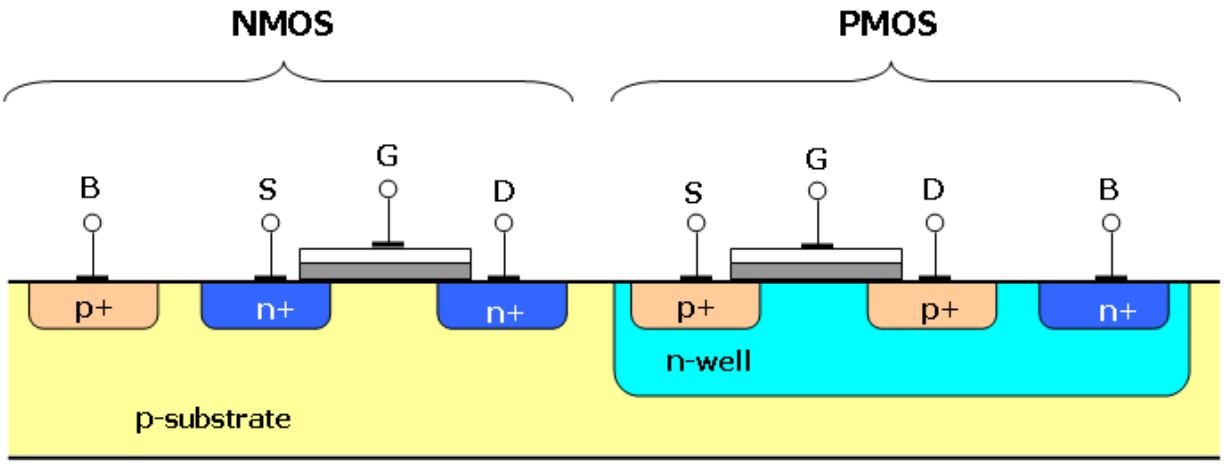

Figure 10: Schematic structure of a CMOS trasistor, consisting of a PMOS and a NMOS [20].

Part II.
Measurment setup

6. MuPix11 chip

The MuPix11 is the final sensor developed for Phase I of the Mu3e experiment. It is a silicon semiconductor detector based on the HV-MAPS technology. This section explains the structure of HV-MAPS and the design of the MuPix11.

6.1. HV-MAPS

The High-Voltage Monolithic Active Pixel Sensor (HV-MAPS) technology is able to perform measurements with precise timing and spatial resolution, while also handling high rates and minimize material budget. HV-MAPS are based on high-voltage CMOS technology, which is readily available due to its use in the industry.
HV-MAPS are based on the charge collection in the deep depletion zone of a diode in reverse bias. Due to ionization electrons get excited in a higher energy state, resulting in a electron-hole pair in the semiconductor. Electron-hole pairs in the depletion zone are separated due to the electric field there. The moving particles induces a signal in the electrodes, which can be measured. If electron-hole pairs are produced outside the depletion zone, they move randomly

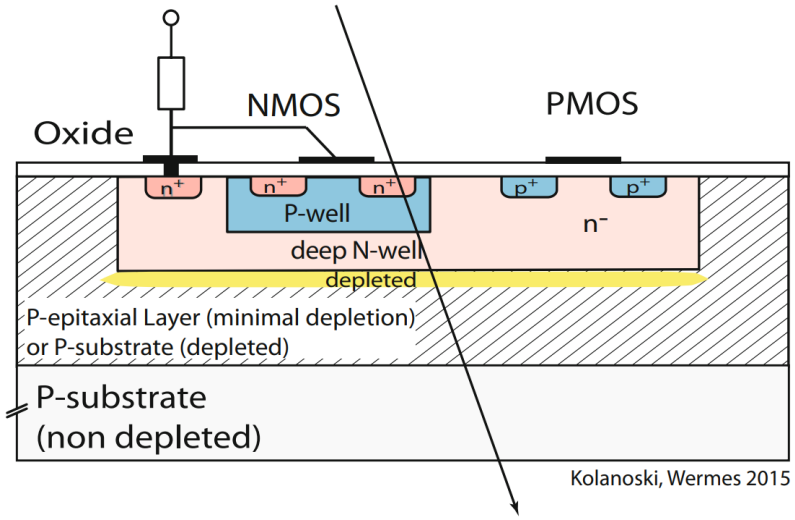

Figure 11: Schematic of a HV-MAPS particle detector [11].

due to diffusion. After some time they recombine or reach the depletion zone.
The high-voltage CMOS technology allows to combine the semiconductor detector diode and the readout electronics on one silicon bulk (monolithic). The diode is formed by a deep n-well in a p-substrate, while the readout electronics are integrated in the shallow n-well (see Figure 11). Both together are called a pixel. The applied high-voltage increases the depleted volume and reduces the charge collection time. This provides a fast signal formation and a more precise time resolution. The non-depleted volume of the p-substrate on the backside is not necessary for the functionality of the sensors and can be removed. It is possible to reduce the thickness of HV-MAPS down to 50 µm.
In one p-substrate multiple pixels can be built in. With this matrix structure the spatial resolution is determined by the size of the pixels and their spacing. For pixel sensors with little or no charge sharing the spatial resolution is approximated by

$$\sigma_{spatial} = \frac{a}{\sqrt{12}}, \tag{7}$$

"a" being the pixel pitch (see Appendix E.1 in [11]). The Mu3e experiment is an example of a experiment that is driving the technology forward in order to improve and further develop it [11, 21].

6.2. MuPix11

The main requirements for Mu3e and the main specifications of the MuPix11 are listed in Table 3 and Table 4, respectively. In the experiment 70 µm and 50 µm thick sensors with 370 Ωcm will be used.
Figure 12 shows the MuPix11 chip layout. The whole sensor is divided into an active area, which is divided into three submatrices, and the periphery. The state machine is located in the periphery, containing of the clocked circuitry to digitize and readout the pixel hits as well as the digital-to-analogue converters (DAC) to control the analogue circuits.

sensor size [mm^2]	20.66×23.18
pixel size [µm^2]	80×80
columns x rows	256 x 250
active area [mm^2]	20.48 × 20
sensor thinned to thickness [µm^2]	50
LVDS links	3+1
maximum bandwidth [Gbit/s]	3×1.25

Table 4: MuPix11 specification from [22].

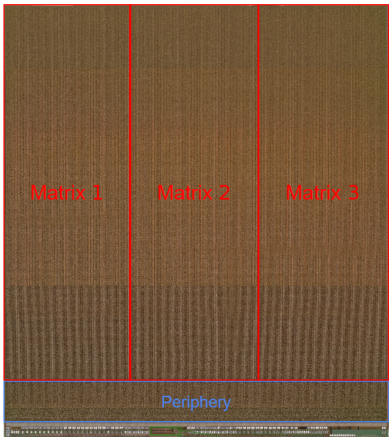

Figure 12: MuPix11 chip divided into matrix 1, 2 and 3 corresponding to data link 1, 2 and 3 [23].

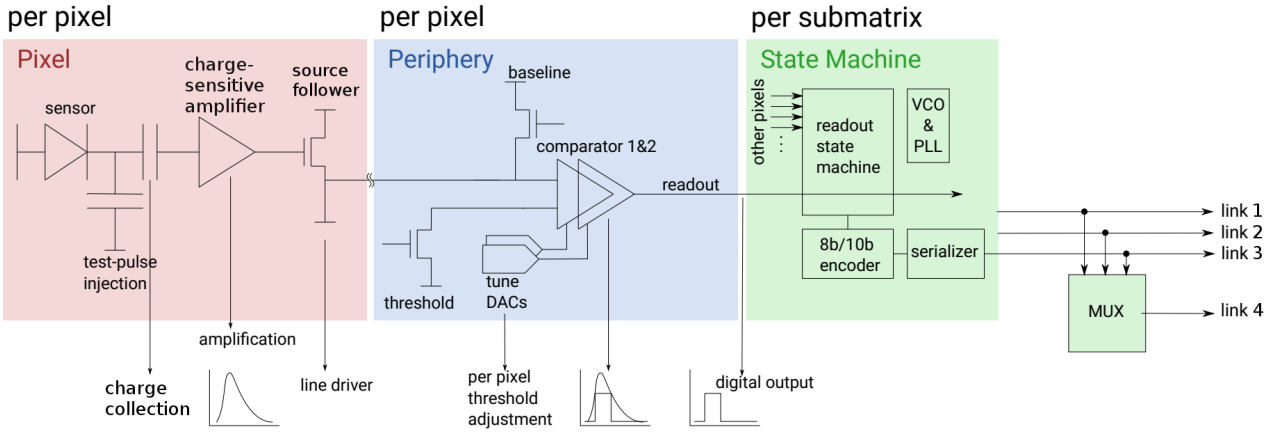

Figure 13: Electronic structure of the MuPix chip [22].

The electronic structure of the sensor is sketched in Figure 13. In each pixel is a charge sensitive amplifier and a source follower, functioning as a line driver. With a capacitor a test charge can be injected into the amplifier system, allowing to simulate a sensor hit for testing and characterisation of the readout.

The voltage for the amplifier is generated in the periphery and called VSSA. Through the additional current from the 1.0-1.2 V network additional heat is dissipated in the periphery of the chip. For each pixel there are two individually adjustable comparators, filtering noise. The time-of-arrival (ToA) is the moment the signal exceeds the threshold and the time-over-threshold (ToT) is the time from ToA to the moment the signal falls below the threshold. A particle with more energy has a "larger" signal and therefore a "larger" ToT (see Figure 14). If for two particles with different energies arrive the diode at the same time, their ToA would differ due to the different signal slopes. The different in the ToA is called "timewalk". With a second threshold a less timewalk affected ToA can be obtained.

The data from each submatrix will be read out, encoded and serialized by an extra state ma-

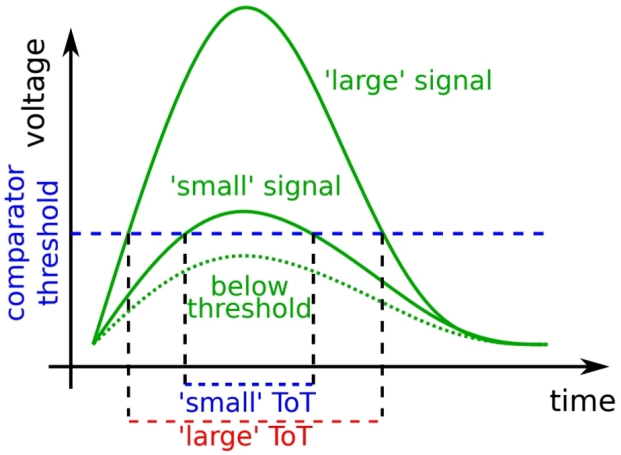

Figure 14: Signals for different particle energies. Smaller energies correspond to smaller signal amplitudes [21].

chine (see subsection 8.1 and subsection 9.1). Their outputs are transmitted via differential data links with 1.25 Gbit/s bandwidth, called link 1,2 and 3 (see subsection 7.1). A link 4 can multiplex the data streams of the three links or mirror one of them.

7. Setup

To measure the data link quality and its behavior a MuPix11 chip is operated in climate controlled environment. In the following section the setup and the functionality of the most important individual part are described in more detail.

7.1. Chip

The MuPix11 chip has four serial data links, hereinafter refereed to as link 1 to 4. Each of this data links can be operated at data rates up to 1.25 Gbit/s. The first three transmit data from different parts of the chip (Figure 12) allowing to handle higher amounts of data, which will be used for the inner parts of the Mu3e detector. Link 4 can be set to mirror the data from one of the other links or multiplex all three of them into one data stream. The multiplex will be used for the outer layers of the Mu3e detector because the hit occupancy there is lower, so the data stream and therefore the needed computing power can be reduced.

7.2. Insert

For the sensor setup a MuPix11 is glued and wire-bonded to a PCB-insert-card. The readout electronics in the periphery of the chip contain the clocked circuitry to digitize and readout the pixel hits and digital-to-analogue converters (DACs). The links on the chip are permanently wire-bonded to the bond pads of the insert, connecting sensor and insert. The insert provides 1.9 V supply voltage to the chip.

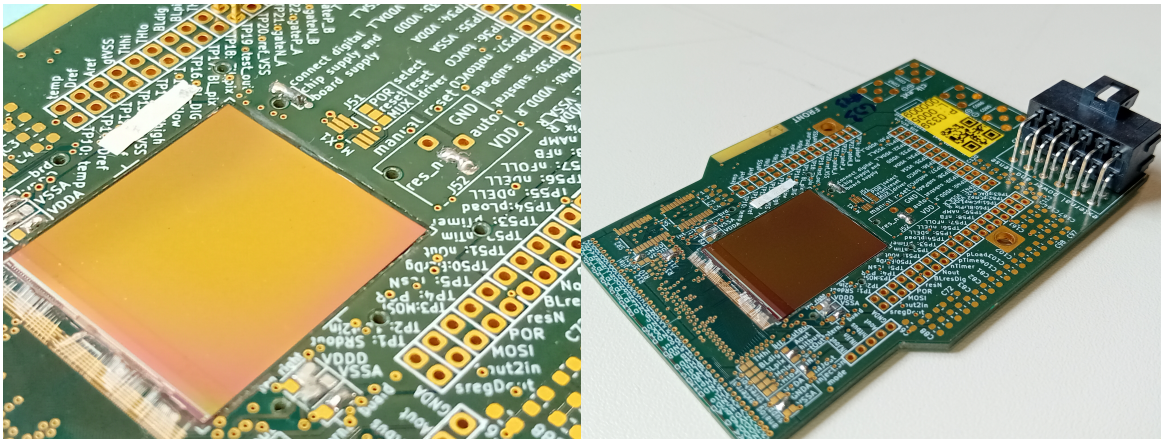

Figure 15: MuPix11 sensor mounted on an Insert card

Figure 16: Full experimental setup

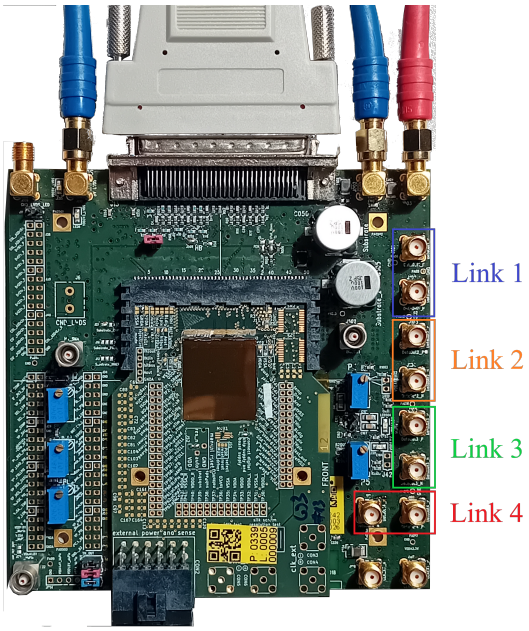

Figure 17: Insert card on motherboard with the SMA connectors assigned to the four data links.

7.3. MuPix8 Motherboard

The motherboard originally developed for MuPix8 are also used for MuPix11. It connects a sensor to an FPGA via SCSI cable, allowing on one hand configuring the electronics on the sensor and on the other hand to process and save the incoming data. The motherboard provides

connections to tap the differential data lines and investigate them with a Digital Serial Analyser. On the board links 1 to 4 are directed by default to the computer for saving and analyzing, but one can reroute every single one of them individually by setting jumper on the back of the board. The redirected differential signal can then be read out at two SMA connectors on the board. For the most measurements link 4 mirroring link 1 is chosen to be rerouted and looked at, so that the 8/10bit-error-free operation of the sensor can be checked via the other links.

7.4. Digital Serial Analyzer

To investigate the signal quality the "Tektronix DSA8300 Digital Serial Analyzer" (DSA) [24] is connected via SMA connectors to pick up the differential signal from link 4. The module "80E04 Sampling Module" [25] is used to pick up the signal. The DSA uses the signal to computes an eye diagram, which allows to quantify signal amplitude, noise, jitter and quality (see subsection 8.2). For the temporal trigger the reference clock is directly connected from the FPGA to the DSA.

7.5. Powering

For the setup there are three sources of power needed:

- The low chip voltage (**LV-chip**) operates the electronics of the chip itself and is directly connected to the insert. The set voltage is 1.9 V, so the required voltage of 1.8 V to operate the sensor is definitely achieved despite the voltage drop to the chips power grid.
- The high voltage (**HV**) is depleting the pixel diodes in the sensor and is connected via the motherboard. The value can be set from 0V (not depleted) to -30 V (fully depleted) for 70 m sensors or -15 V for 50 m. Despite not being fully depleted the sensors still can be operated without problems, e.g. at -15 V, which is the standard setting for the measurements.
- The low board voltage (**LV-board**) supplies the electronics on the motherboard with power. Here 5 V is the value for operating.

The low voltages are supplied by a "Hameg" power supply and the high voltage by a "Keithley".

7.6. FPGA

A field-programmable gate array (FPGA) is connected via PCI Express to a computer and via a SCSI cable to the detector board. It is used on one hand to receive and process the data from the detector, on the other hand to control and configured the electronics, e.g. the DACs. FPGAs are integrated circuits with reprogrammable hardware and customizeable for very different situation. Due to the high speed data transmission (here 1.25 Gbit/s) and its parallel processing capabilities they are used to handle large data streams. In this setup an Altera Stratix IV FPGA development board [26] is used .

7.7. Temperature Measurement

To complete the setup and enable temperature measurements, a cooling chamber is needed, which allows to put the detector inside and still be connected to the other devices outside and is also able to cover the temperature range from -20°C to 80°C, which is the expected range for the detectors in the Mu3e experiment. The device in use is a "Binder 9020-0006 Cold/Heat Material Testing Chamber", capable of setting the temperature between -40°C and 180°C. The cables of the devices outside are connected through a resealable hole to the detector. With a digital thermometer to cross-check the temperature inside the chamber a the bottom, one observes, that to change the temperature by 10K in the whole chamber it takes one hour. Also for temperature measurements, the board is put on a non-conducting porcelain plate to isolate electronics from the metal grid of the cooling chamber.

8. Readout

The data readout goes through a lot of different steps before an output signal arrives at the DSA. In this section, the functions of the state machine and the parameters computed by the DSA are explained in more detail.

8.1. MuPix Data

The information from the sensor are 8/10bit encoded, which means each 8bit of information gets converted to a 10bit transmission character. In the transmission bits only the same numbers of "1" and "0" (5:5) bits or two more than the other (6:4, 4:6) are allowed. To determine the DC component of the serial signal, on average the disparity should be neutral, which means for a differential signal on average there should be the same numbers of "0" and "1" [27]. With this limitations of possibilities for the transmitting bits, deviations trough bit errors can be checked easily. In this case an "8/10bit error" is issued. Such 8/10-bit errors should not occur in a data stream, as they indicate a non-functional setting. To observe the the 8/10bit error rate, link 1 to 3 are read-out and are reviewed for this errors.
The signal is transmitted using low-voltage differential signaling (LVDS). Figure 18 shows a current-mode logic (CML) LVDS driver, used in the MuPix11. The serialized, differential signaling allows to operate at high speed for low power cost. The data is transmitted as the difference between two voltages, conveyed via two different conduction lines. The differential signaling allows the cancellation of electromagnetic noise in the cable and other conducting parts due to the subtraction of the voltages.

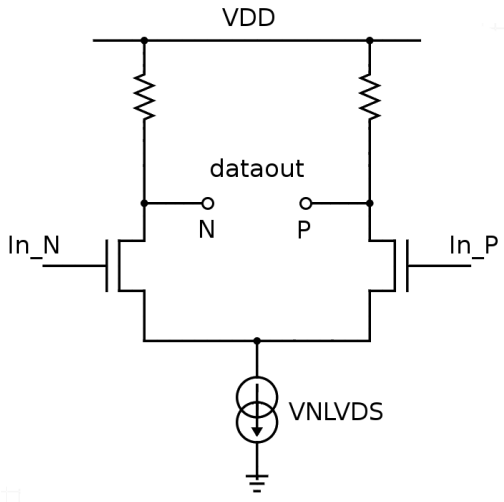

Figure 18: Circuit diagram of the LVDS driver (CML mode).

8.2. Eye diagrams

To measure the signal quality of the signal from the sensor, a Digital Serial Analyzer is used. It is able to compute "eye diagrams", which are graphical overlays of the same signal at different times. The sampled signal is divided into subframes with the length of one bit. For an ideal bit sequence, where the transitions from a logical "0" to "1" and vice versa are instantaneous (Figure 19a), the length would be exactly one bit. For a real bit sequence, where the transitions are more "rounded" due to the time capacitors need to charge and discharge (Figure 19b), the length of the subframes can varies. Through the overlay of the subframes a pattern looking like an eye is created. Figure 22 shows this pattern for all possible variations of a real 3-bit sequence. For stable signals the subframe lengths are very similar and overly to an wide "open" eye. If the signal strongly varies in its transition, the rising and falling signal lines defining the eyes are broader and therefore the eye is more "closed". For an closed eye the difference between the logical "0" and "1" is not distinguishable. Figure 21 shows two eye diagrams with

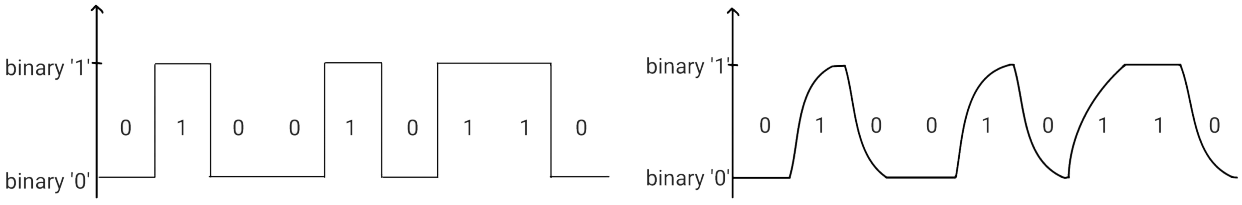

(a) ideal (b) real

Figure 19: Schematic overview of an (a) ideal and a (b) real bit sequence.

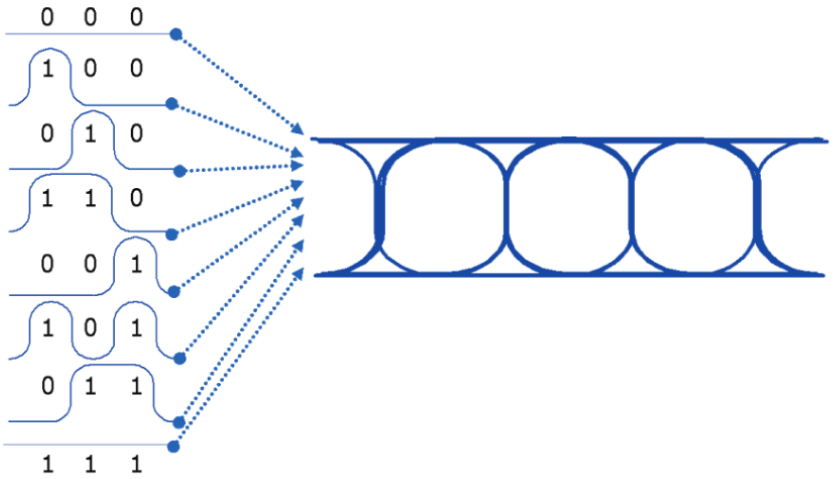

Figure 20: Schematic overlaying of different 3-bit sequence into an eye diagram [28].

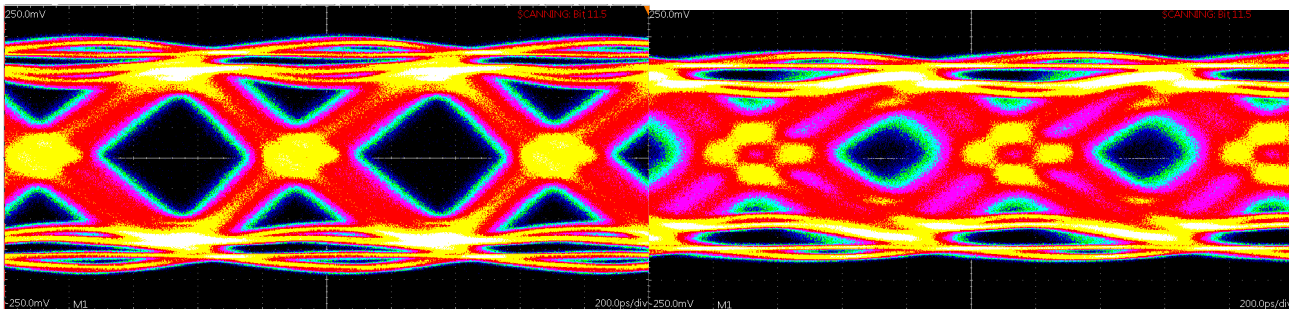

Figure 21: Eye diagrams of two different settings.

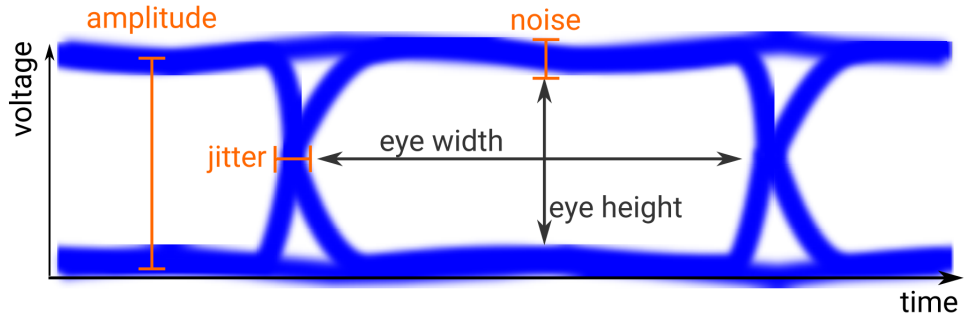

Figure 22: Sketch of an eye diagram with the most important parameters indicated [29].

different configurations. The one on the left has clear open eyes and therefore a stable signal, while the one on the right is barley open and therefore an unstable signal. To compare different settings of the sensor as well as different external influences, the following four parameters are introduced:

Amplitude The difference between the logical "1" level (High) and the logical "0" level (Low) of the signal.

$$\text{Amplitude} = \text{High} - \text{Low} \tag{8}$$

Eye Height A measure of how noise affects the vertical opening between the High and Low levels of an eye. The noise levels are characterized by σ_{high} and σ_{low}, the standard deviations from the mean for the High and Low levels.

$$\text{Eye Height} = (\text{High} - 3 \cdot \sigma_{\text{high}}) - (\text{Low} + 3 \cdot \sigma_{\text{low}}) \tag{9}$$

Eye Width A measure of how jitter affects the horizontal opening between two consecutive eye crossings. The two crossings T_{cross1} and T_{cross2} are calculated by the mean of the histogram. The jitter levels are characterized by σ_{cross1} and σ_{cross2}, the standard deviations from the

mean for the crossings.

$$\text{Eye Width} = (T_{\text{cross2}} - 3 \cdot \sigma_{\text{cross2}}) - (T_{\text{cross1}} + 3 \cdot \sigma_{\text{cross1}}) \tag{10}$$

Q-factor A figure of merit of an eye diagram, reporting the ratio between the amplitude of the eye to the total RMS(root-mean-square) noise on the High and Low levels. The noise levels are characterized by σ_{high} and σ_{low}, the standard deviations from the mean for the High and Low levels. The Q-factor is a typical value for the quality of a signal.

$$\text{Q-factor} = (\text{High} - \text{Low})/(\sigma_{\text{high}} + \sigma_{\text{low}}) \tag{11}$$

By using 5000 measurements the statistical error of these parameters from the DSA is far below 1 % and therefore negligible. The uncertainty of the vertical voltage measurement is determined by the "80E04 Sampling Module" [25] and the horizontal time measurement by the Stratix IV FPGA clock resolution.

Part III.
Measurments of the data links

In this part the measurements and the results obtained with the previously described setup are discussed. The measurements taken are focused on the quality of the signal of the data links and its dependencies on the settings of the DACs on the sensor and on the temperature. Two 70 µm and one 50 µm thick Mupix11 sensor are used to perform the measurements, further referenced as MP11-70-1, MP11-70-2 and MP11-50.

9. Variation of DAC values

The settings of the digital components are controlled by the digital to analogue converters (DACs). To understand the influence these DAC settings have on the signal, the eye diagrams for different DAC variations are observed via the DSA. In this chapter, first an overview of the DACs is given. Afterward the results of the investigated DACs are presented and discussed.

9.1. Overview of the DACs

A signal from the sensor is transmitted to the serializing logic before reaching the output links. The serializing logic fulfills different task to process the incoming signal. Part thereof is the 8/10bit encoder as well as the differential current mode logic (Dcl) serializer, converting parallel data into serial data. The phase-locked loop (PLL) synchronizes the external reference clock (from the FPGA) with the internal clock, getting distributed by the clock generation tree to the Dcl serializer [30]. The whole readout process is schematically shown in Figure 23.
The logical blocks are controlled with adjustable voltages. These so called DACs have a dynamic range from 0 to 63, referring to the amount of current allowed to flow through the DACs. The value of 0 correspond to a current of 0, while 63 correspond to the maximal possible amount of current. Over the time a default set of values for all parameter was established for the MuPix11 sensor to operate smoothly, further refereed to as "standard configuration". The DACs investigated in this thesis and their standard configuration are summed up in Table 5.
To investigate the influence of different DAC values on the signal quality of the data link, one of the values gets varied relative to its standard, while the others are kept on their standard

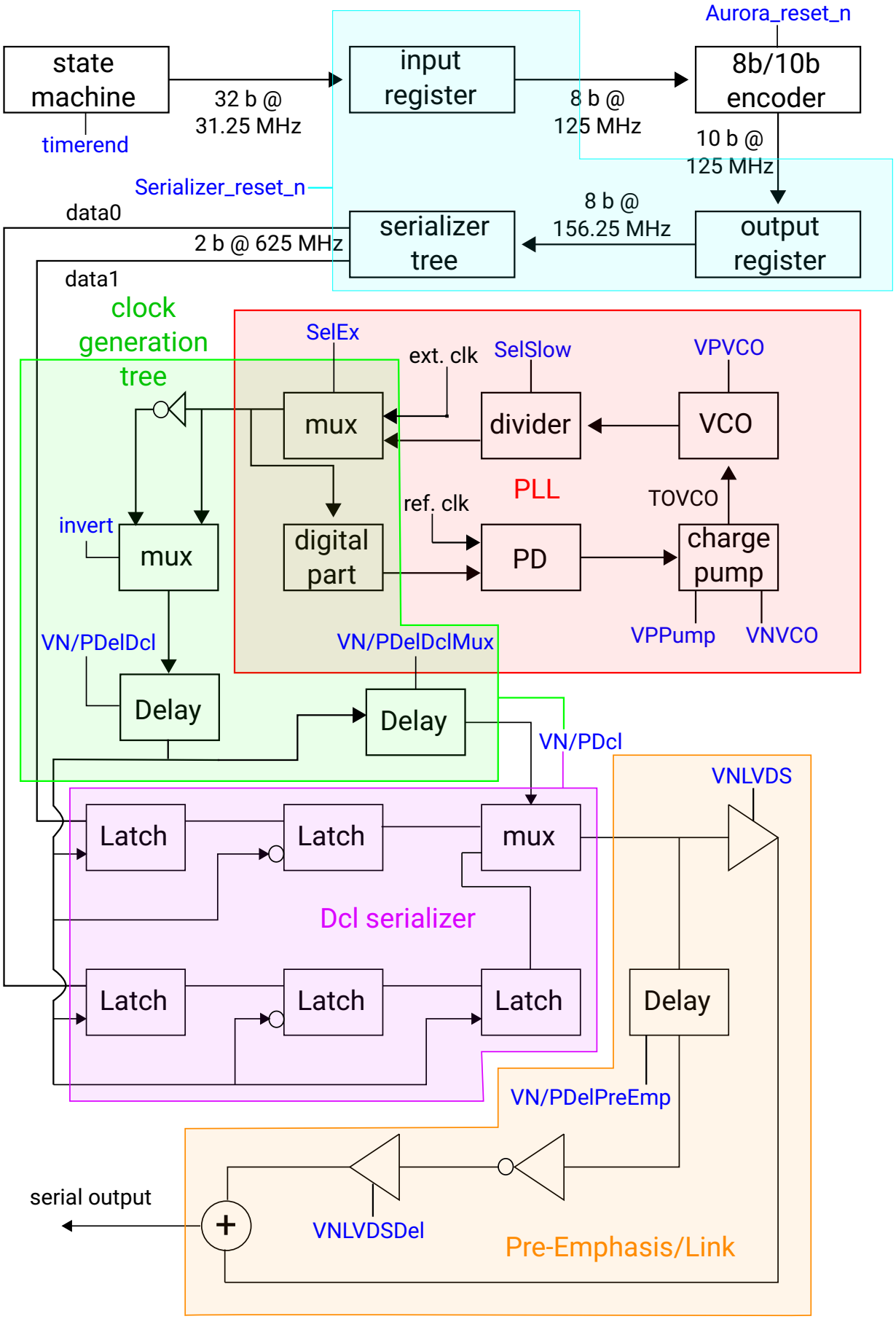

Figure 23: Readout state machine scheme [30].

DAC	default configuration	Function
VPDcl	30	Global Dcl bias
VNDcl	15	Global Dcl bias
VNLVDS	15	Strength of link buffer
VPDelDcl	10	Delay for Dcl clock
VNDelDcl	10	Delay for Dcl clock
VPDelDclMux	10	Delay for Dcl mux clock
VNDelDclMux	10	Delay for Dcl mux clock
VPDelPreEmp	10	Delay of pre-emphasis
VPDelPreEmp	10	Delay of pre-emphasis
VNLVDSDel	0	Strength of pre-emphasis buffer
VPPump	63	Charge Pump Bias

Table 5: Different DACs, their default value in decimal numbers and their function. Adapted from [30].

value. The smallest and the highest value measured sets the minimum and maximum the sensor can be operated without observing 8/10bit errors. The measurement is performed with the MP11-70-1 sensor at room temperature via link 4 mirroring link 1.
The increase or decrease of the chip power consumption is mentioned for DACs having an influence of more than 1% over the whole range. The power consumption of the sensor can be determined by multiplying the chip supply voltage (chip LV) with the chip supply current.

9.2. VN/VPDcl variations

VNDcl and VPDcl are the global Dcl bias, controlling the overall current in the Dcl serializer and the clock generation tree. Empirically, both DACs should be changed simultaneous for optimized operation. The values of the eye parameters for the variation of VPDcl and VNDcl are shown in Figure 24.
The amplitude for VPDcl is the highest for its default value 30, for smaller values it decreases as well as for larger ones. The decrease for smaller values is expected because decreasing the Dcl bias reduces the current and therefore the signal amplitude. This happens till there is not enough current to operate the Dcl serializer. The decrease for higher values occur due to the increasing difference between VNDcl and VPDcl.
The amplitudes for VNDcl behave similar to the ones of VPDcl, but the values for the amplitude stay relatively constant from 15 to 39 and only drops for too small values, where the current beginns to switch off. The DAC value of 42 is the upper limit for the measurements of the eye diagrams because for higher values 8/10bit errors occur disturbing the measurment of

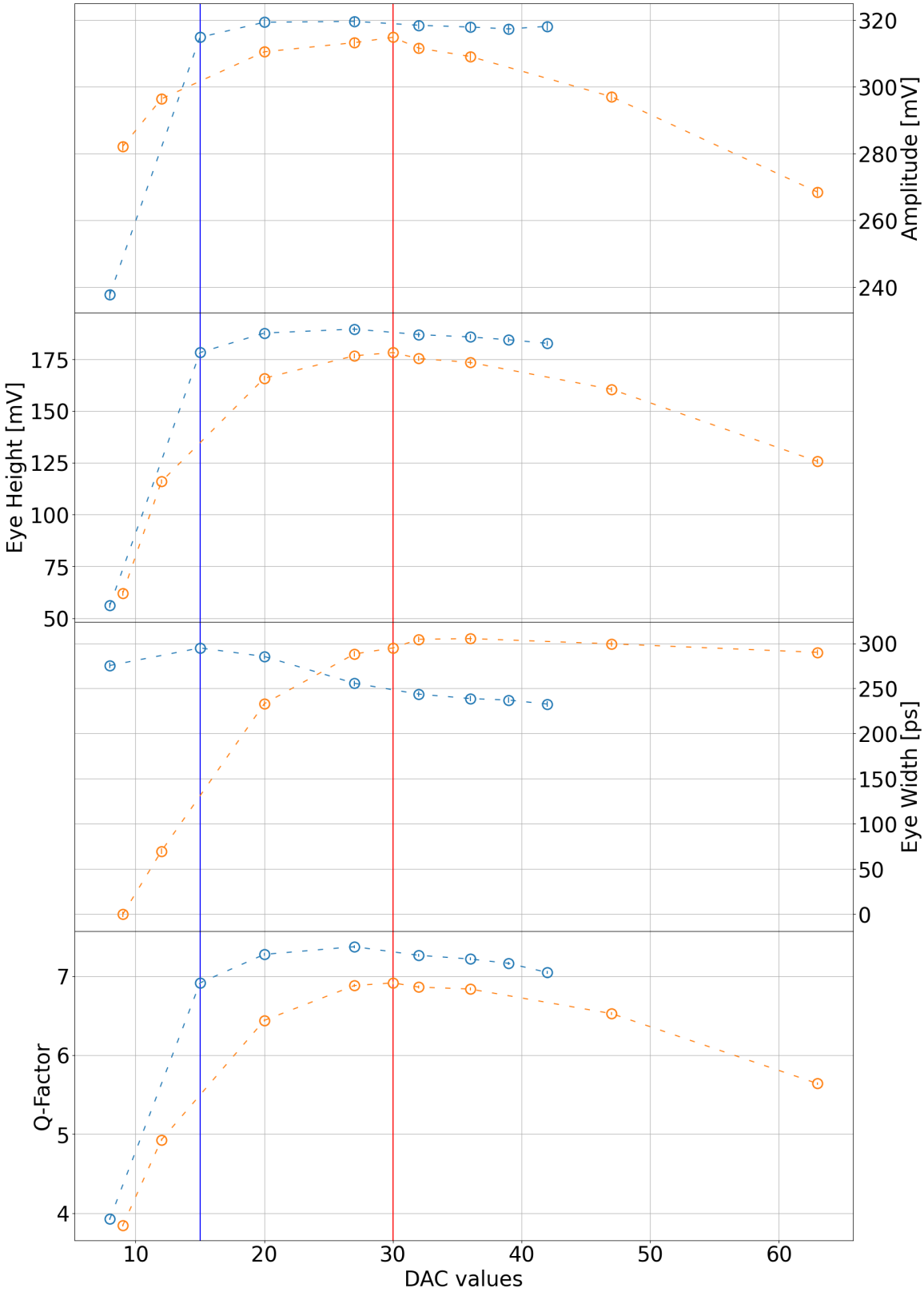

Figure 24: Eye parameter for different DAC values of VPDcl (orange) and VNDcl (blue). The vertical red line indicates the standard value for VPDcl and the blue one for VNDcl.

the eye. This could be due to the difference of the default values of VPDcl and VNDcl.
The eye heights of both DACs look very similar to the amplitudes because the noise does not change significant as long as the system is stable. For VNDcl the system gets unstable for DAC values <15, where the amplitude drops by $\sim$ 25%. The noise increases and therefore the eye height drop is relatively larger with $\sim$ 70%.
For higher values of the VPDcl the setup is still stable and the eye width is relatively constant. In contrast it decreases strongly for DAC values below 28 till the eye width is 0. Judging from the eye diagrams of the two lowest values (Figure 25) the computation of the eye width from the crossing times and jitter did not work properly because of the recangle structure with a hole in it, where normally would be only one crossing. The VPDcl seems to influence the timing resulting in a constant delay and therefore this parallel structure. For higher values of VPDcl the delay vanishes and the eye width can be calculated.
For the VNDcl the eyewidth is decreasing by $\sim$100 ps for higher DAC values as the default, but

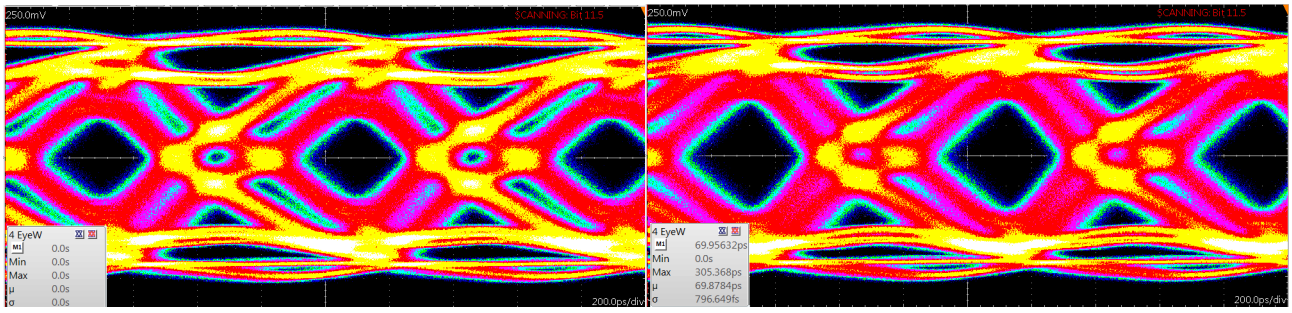

(a) 9 (b) 12

Figure 25: Eye diagrams for VPDcl set to 9 and 12.

for the smaller DAC values, where the amplitude begins to drop, the eye width only decreases by $\sim$25 ps. Here is no problem like for VPDcl for small values, maybe because the powering of the Dcl serializer is covered by the VPDcl for small VNDcl, while in reverse the default bias of VNDcl is not enough to cover small VPDcl values.
The Q-factors have a similar structure to the eye heights of both DACs. For the VPDcl the default value is already the best Q-factor and sits on a plateau, making it a good and stable setting. The default value for the VNDcl on the other hand doesn't produce the best Q-factor, but lays at the beginning of an plateau. Choosing a higher DAC value at around 27, the amplitude to noise ratio improves and therefore a better signal quality can be achieved.
For VPDcl the overall power consumption increases from the default value of 30 to 63 by around 2.9 mW (0.4 %) and decreases from the default to 9 by around 4.7 mW (0.7 %). For VNDcl the overall power consumption increases from the default value of 15 to 42 by around 54.9 mW (7.6 %) and decreases from the default to 8 by around 21.1 mW (2.9 %).

9.3. VNLVDS variation

VNLVDS is the strength of the link buffer, controlling the amount of output current in the links. The values of the eye parameters for the variation of VNLVDS are shown in Figure 27 (blue). For low DAC values the digital buffer blocks the incoming signal, reducing the amplitude down to 50 mV. For values higher as the default value of 15, the amplitude increases just by about 50 mV and saturates at a value of 36.
The eye height behaves similar. For low values the the amplitude is small, but there is also little noise. Approaching the default value the amplitude increases, but also the noise increases. Reaching the point of saturation the eye height stays constant, meaning the noise does not increase anymore like the amplitude, which makes sense considering a digital buffer to maintain the signal integrity.
The Q-factor overall changes only by around 0.4, neglecting the one value at 1. The Q-factor at 5 is the highest value achieved, but it corresponds to an amplitude of only about 175 mV compared to the about 310 mV for the standard configuration.Therefore the increase of around 0.15 in the Q-factor does not seem to be worth if the amplitude is halves for this. For higher values the decrease of the Q-factor is also only around 0.25, but here the amplitude does not increase to much, making the DAC value of 15 a good default.
The digital buffer does not effect the eye width because it should maintaining signal integrity and ensuring proper communication between different parts of a digital system, not influencing the the timing or jitter. But the rising and falling time of a signal can be faster for small amplitudes, decreasing the eye width and increasing the jitter. In Figure 26 the top half of the eye diagram for a DAC value of 5 and the bottom half of the eye diagram for a DAC value of 63 are put over each other. One can see the smaller eye width for the lower amplitude compared to the bigger amplitude, but the difference of ∼20 ps is negligible compared to the crossing to crossing distance of ∼800 ps and to the eye width of ∼300 ps.
The overall power consumption increases from the default value of 15 to 63 by around 41.6 mW (5.8 %) and decreases from the default to 1 by around 43.9 mW (6.1 %).

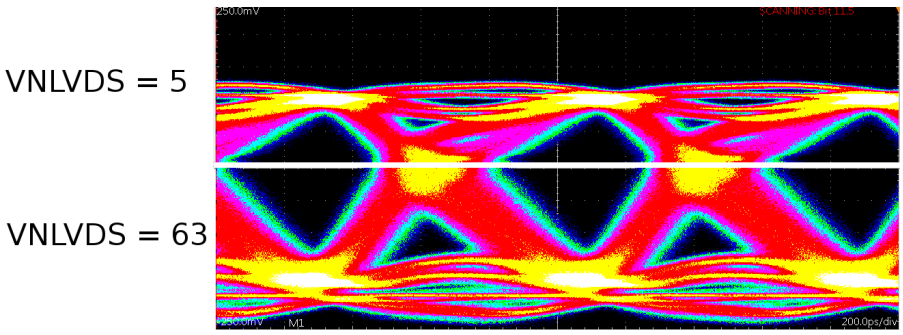

Figure 26: Comparison of the eye width for VNLVDS 5 (top part) and 63 (bottom part)

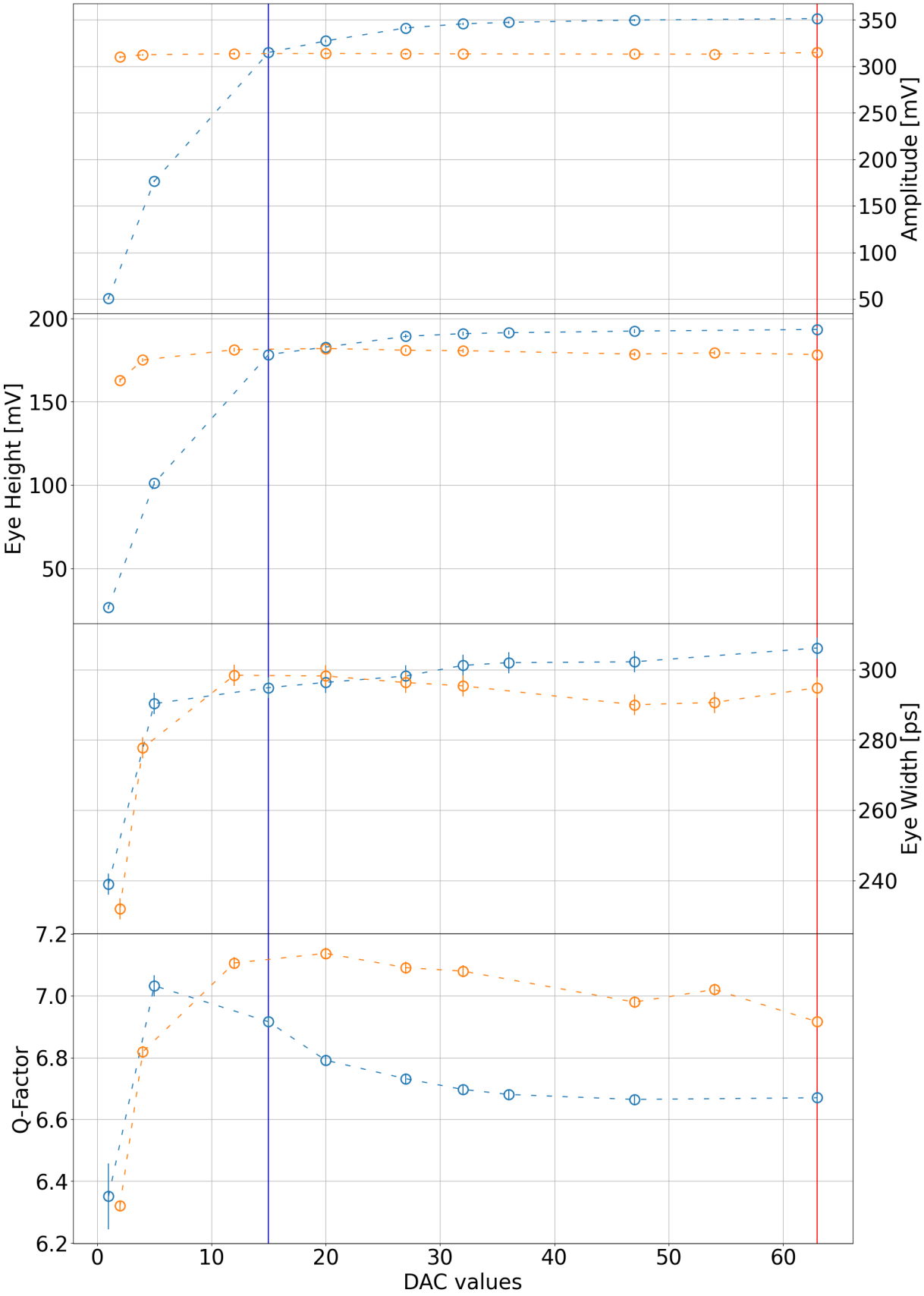

Figure 27: Eye parameter for different DAC values of VPPump (orange) and VNLVDS (blue). The vertical blue line indicates the standard value for VPPump and the red one for VNLVDS.

9.4. VPPump variation

If the internal clock is out of sync with the external clock, the PLL needs to correct the shift. The VPPump DAC controls the bias of the charge pumpand therefore the step size of these correction. A higher bias correspond to a higher step size. For too large step sizes the correction can be overdone, resulting in a new shift, while for too step sizes the correction can be too slow before new asynchronizations appear. The values of the eye parameters for the variation of VPPump are shown in Figure 27 (orange).
The eye width should decrease for small DAC values, which happens for values <12. For values ≥12 the eye width stays approximately constant (fluctuations of ∼10 ps, which is negligible small) due to faster regulation.
Primarily influencing the timing, the VPPumpp doesn't affect the amplitude. For DAC values <12 the eye height drops by ∼20 mV, indicating a small increase of noise. The Q-factor therefore drops the strongest for DAC values <12. But lowering the default and maximal value of 63 to 12 there is an increase of the Q-factor by ∼0.1 to 0.2, which is only an increase by ∼2%-3%. Considering there is no lose of amplitude or increase of noise, one can still adapt the vale of VPPump to for example 20 or 48.

9.5. VP/VNDelDclMux variation

VPDelDclMux and VNDelDclMux are located in the clock generation tree and control the delay of the multiplexer in the Dcl serializer. The values of their eye parameters are shown in Figure 28. The amplitude is within the errors constant for both DACs since they control the delay. Only for VNDelDclMux DAC values over 48 the amplitude drops by around 7 mV (2%). Also the values of the eye height and the Q-factor decrease for higher DAC values, indicating a malfunction and increase of noise in the logical block controlled by the VPDelDclMux for too high voltages. The same effect also occurs weaker for DAC values under 10.
The eye width for VNDelDclMux decrease for DAC values different than the default value of 10. The delay determines the overlay of different signals and therefore define (among other DACs) the jitter. So there is a range of DAC values optimal for the operation of the DAC, here around the default value of 10. For VPDelDclMux the range of constant eye width and therefore optimal operation is from 10 to around 39 and decrease outside this range due to too strong or too weak delay.
Overall VPDelDclMux and VNDelDclMux performe the best for their default value of 10.

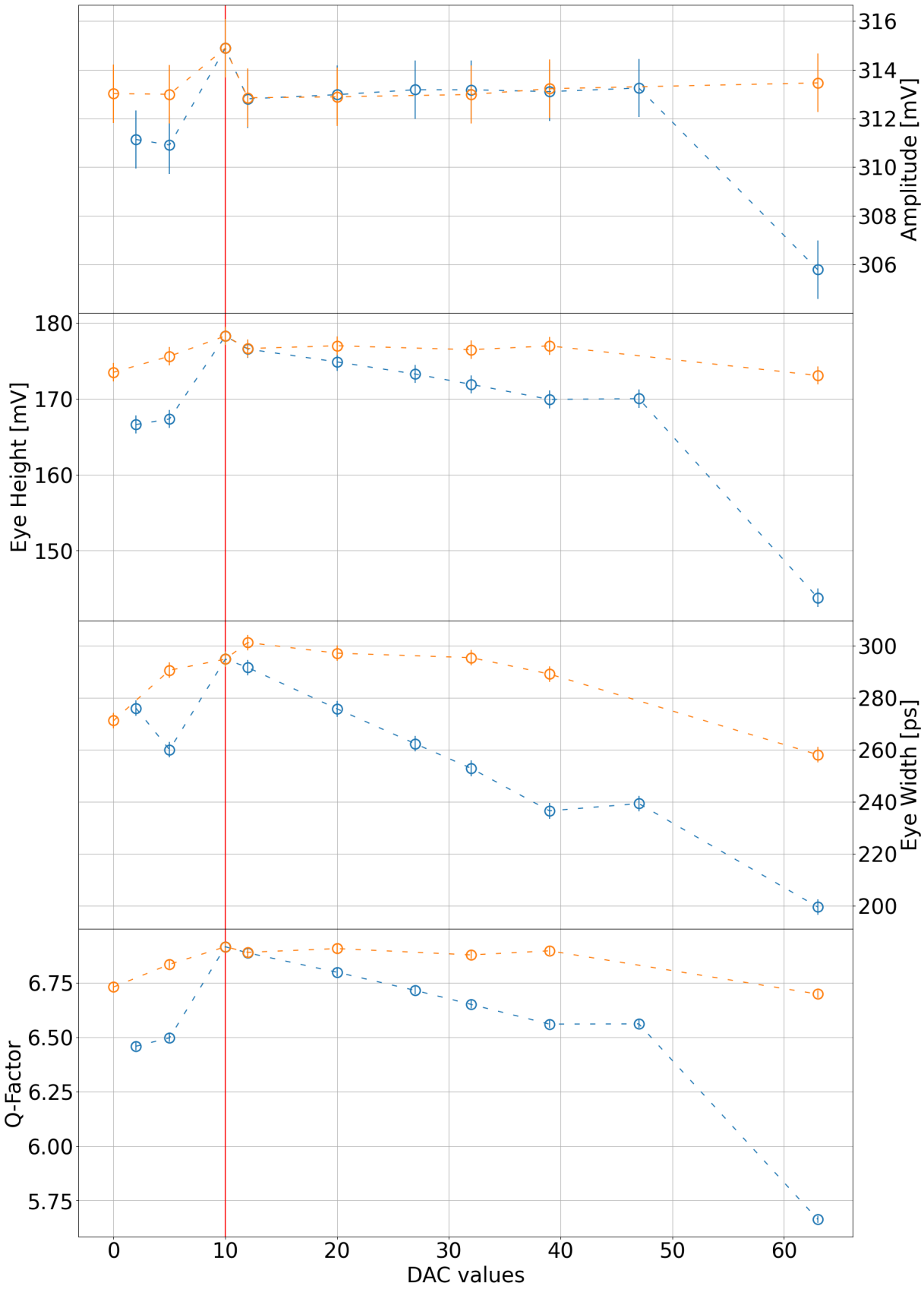

Figure 28: Eye parameter for different DAC values of VPDelDclMux (orange) and VNDelDclMux (blue). The vertical red line indicates the standard value for VPDelDclMux and VNDelDclMux.

9.6. VP/VNDelDcl variation

The DelDcls adjust the Dcl delay in the clock generation tree. The values of the eye parameters for the variation of VPDelDcl and VNDelDcl are shown in Figure 29. Only affecting the delay the amplitude and the eye height, and therefore also the Q-factor, are not affected by change of these DACs within the error range. Compared to the DelDclMux DAC, VPDelDcl and VNDelDcl each only control the delay of one of the differential lines. Changing the DACs one at the time does not influence the eye parameters by more than around 1% and has no systematic behavior. The default DAC value of 10 is a good default for VNDelDcl, while a DAC value of around 12 can improve the Q-factor of VPDelDcl by around 0.1.

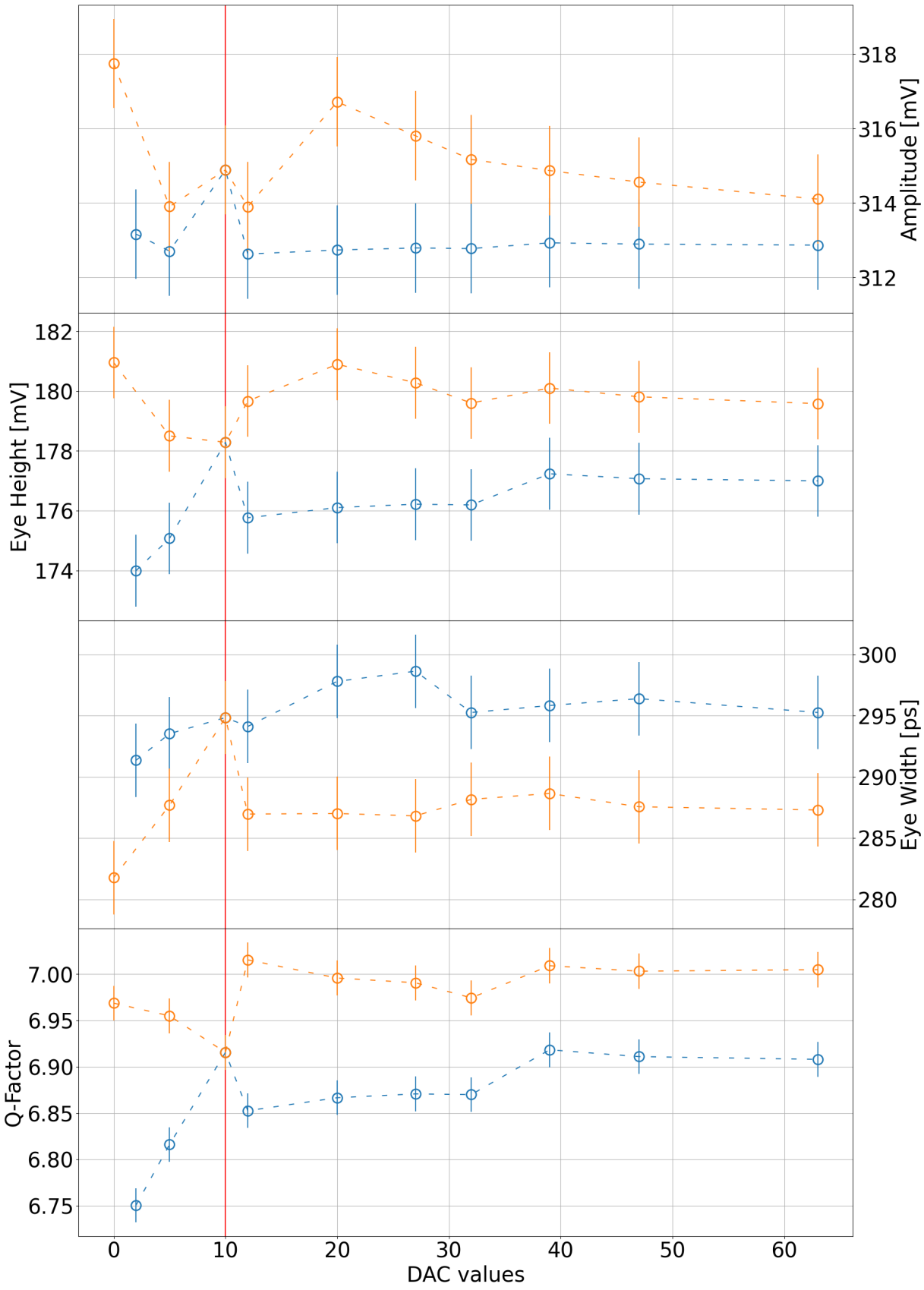

Figure 29: Eye parameter for different DAC values of VPDelDcl (orange) and VNDelDcl (blue). The vertical red line indicates the standard value for VPDelDcl and VNDelDcl.

10. Temperature variations

In this section the influence of the ambient temperature on the HV current, the power consumption, the VDD of the chip and the eye parameter will be investigated. The 70 µm thick MP11-70-2 and the 50 µm thick MP-50 sensors are put in the cooling chamber and get exposed to an ambient temperature range from −20 °C to 80 °C. The DACs are set to the standard configuration (Table 5).

10.1. HV current limit

During the temperature measurements the current of the HV is observed for MP11-70-1 and MP11-50 with increasing temperature. The current can be read of directly at the power supply. For both sensors the HV depleting the semiconductors in the sensor is initially −15 V. The current in the silicon diodes should not exceed the value of 100 µA, else thermal runaway can occur and affects the sensor performance. The temperature dependence of the leakage current in a diode is according to Equation 6:

$$I_L \sim T^2 \cdot e^{-1/T},$$

where the exponential function is the dominant term.
Figure 30 shows the HV current during the measurement of the eye parameter for the temperature range from −20 °C to 80 °C. For MP11-70-1 the (negative) current increases as expected exponentially with increasing temperature. For −15 V 70 µm thick sensors are not fully depleted. From −20 °C to 70 °C the current is below the limit of 100 µA. For 80 °C the limit is reached and the HV needs to get adjusted. The temperature on the chip is due to self heating higher than the ambient temperature. For 70 °C ambient temperature and around 400 mA LV current, the chip is approximately 25 °C hotter [31], meaning for 80 °C ambient temperature the sensor is already much hotter than the sensor temperature expected for the Mu3e experiment.
For MP11-50 the (negative) current also increases as expected exponentially with increasing temperature. For −15 V the 50 µm thick sensors are fully depleted and therefore this is the maximal HV to apply. Additionally, the 50 µm thick MuPix11s are much more light sensitive than the 70 µm ones, resulting in a higher leakage current in the presence of light. The light source in the climate chamber is covered, but it is still possible the sensor gets illuminated.
With −15 V the MP11-50 reaches the limit before 40 °C, so the voltage needs to be adjusted. For −8 V the limit is not reached at 80 °C. Considering the self heat of the sensor this is an

exceptional high chip temperature for the MP11-50. The 70 °C chip temperature is already reached for around 30 °C to 40 °C ambient temperature, and therefore the voltage can be more than −8 V.

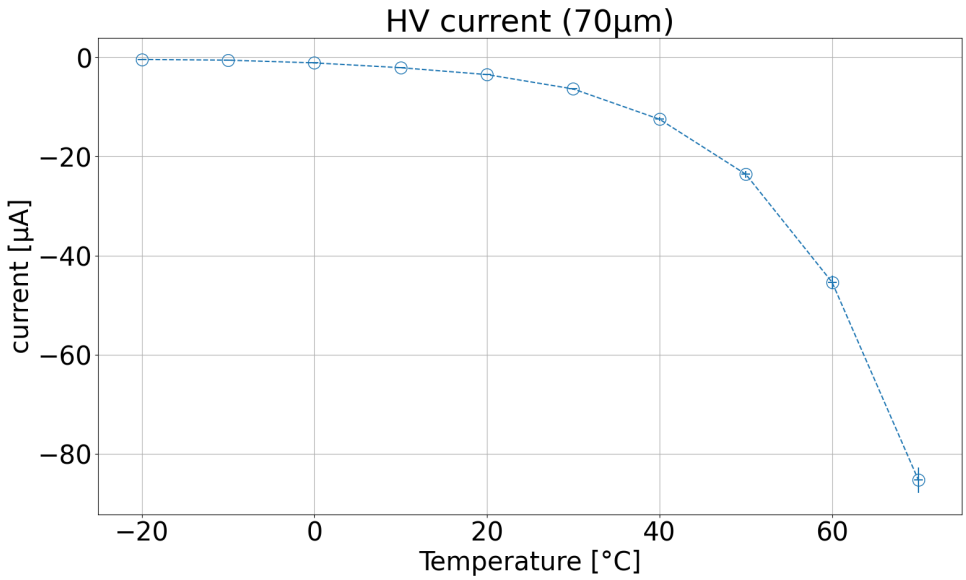

(a) MP11-70-1

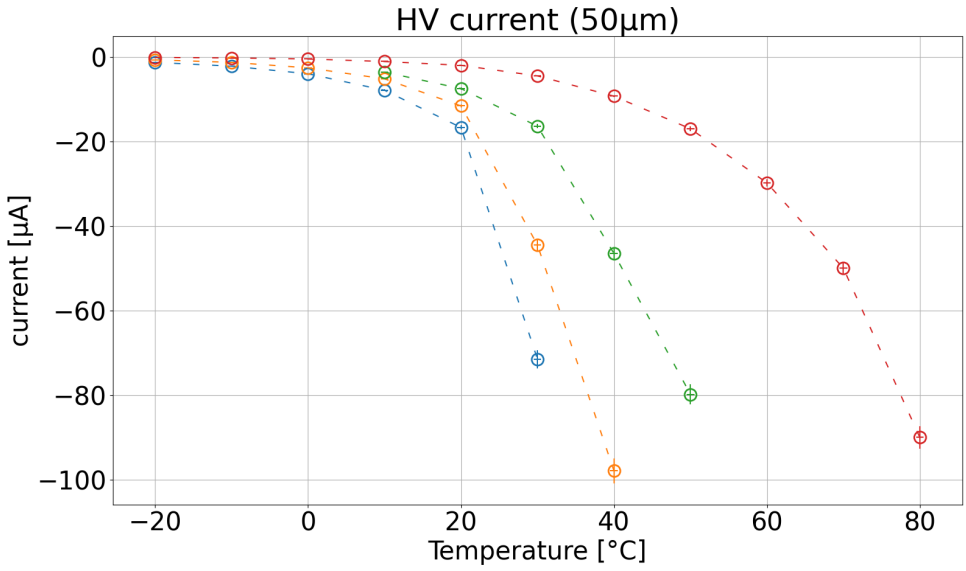

(b) MP11-50

Figure 30: HV current as a function of the temperature for MP11-70-1 and MP11-50. For MP11-50 HVs of −15 V (blue), −12 V (orange), −10 V (green) and −8 V (red) are investigated.

10.2. Chip power consumption

The power consumption of the sensor can be determined by multiplying the chip supply voltage (chip LV) with the chip supply current. During the temperature measurements the current of the chip supply voltage is observed for MP11-70-2 and MP11-50 with increasing temperature (Figure 31). The current can be read of directly at the power supply. For MP11-70-2 the current increases approximately linear with increasing ambient temperature. The complete increase is around 30.3 mA (around 8%), corresponding to an increase in power consumption of around

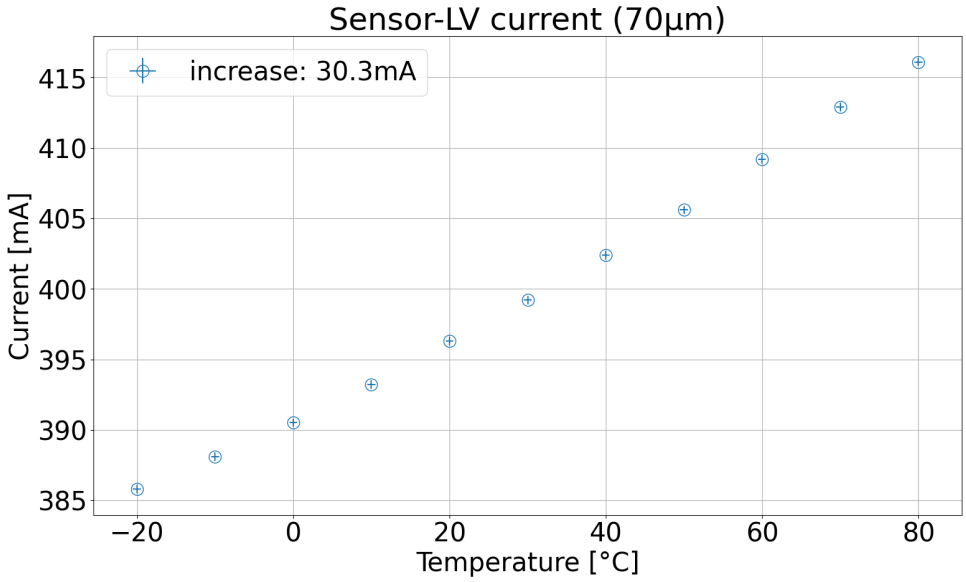

(a) MP11-70-2

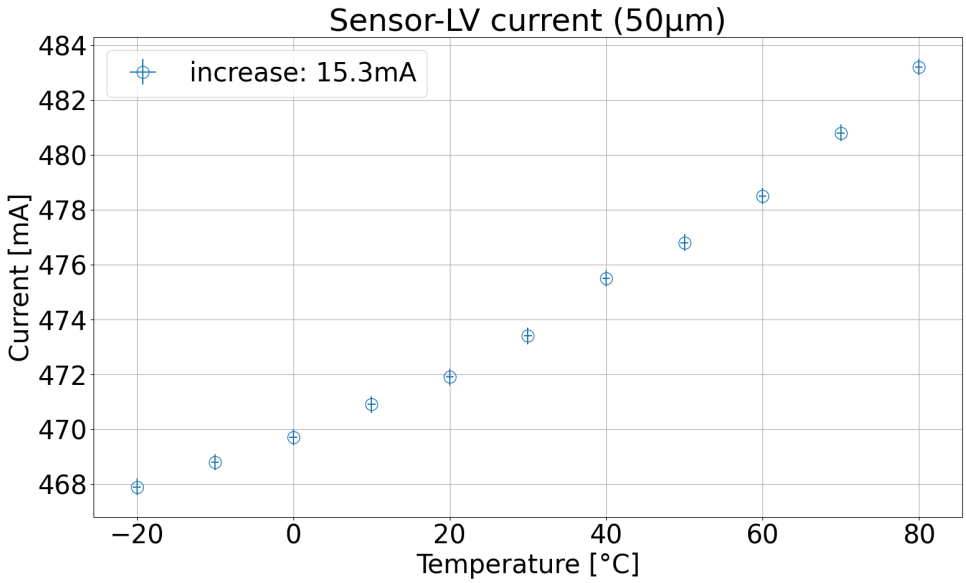

(b) MP11-50

Figure 31: Current of the chip supply voltage of 1.9 V with increasing temperature.

57.6 mW. The current for MP11-50 increases roughly exponential due to the stronger self heating of the 50 µm sensor compared to the 70 µm one [31]. The complete increase is around 15.3 mA (around 3%), corresponding to an increase in power consumption of around 29.1 mW. The difference in increase as well as the difference in absolute values for both thicknesses (MP11-70-2: around 385 mA-417 mA, MP11-50: around 468 mA-483 mA; both from −20 °C to 80 °C) are sensor specific chip-to-chip variations.

10.3. VDD drop

The VDD is the positive supply voltage of MOS circuits. For the MuPix11 sensors the voltage is present from the bond pads to the power grid. The voltages get read out with a multimeter connected to a "test_out" connection on the insert-PCB. There the output can be set to two VDDs and two corresponding GNDs. The difference between the two VDDs, VDD1 and VDD2, and the two GNDs, GND1 and GND2, are the different locations on the chip they get measured. Subtracting the GND from the corresponding VDD should result in a voltage higher than 1.8 V, the minimal supply voltage to operate the sensor.
During the temperature measurements the VDD is observed for MP11-70-2 and MP11-50 with increasing temperature on the sensors (Figure 32). For both sensors and for both locations the voltages decrease linear within the error range with increasing temperature. The drops are for MP11-70-2: 24 ± 4 mV (VDD1) and 22 ± 4 mV (VDD2), and for MP11-50: 22 ± 4 mV (VDD1) and 21 ± 4 mV (VDD2), so equally within the error. The decrease originates from the increase in the senor LV current, observed in subsection 10.2. An increase of the resistivity of metal conductors and resistors in the setup due to the increasing temperature can also have an effect. The difference in absolute values of the voltages for MP11-70-2 (1.857 ± 0.004 V at −20 °C) and MP11-50 (1.844 ± 0.004 V at −20 °C) comes from chip-to-chip variations.
Despite the decrease, all VDDs are still over the 1.8 V, providing enough voltage to operate the sensors.

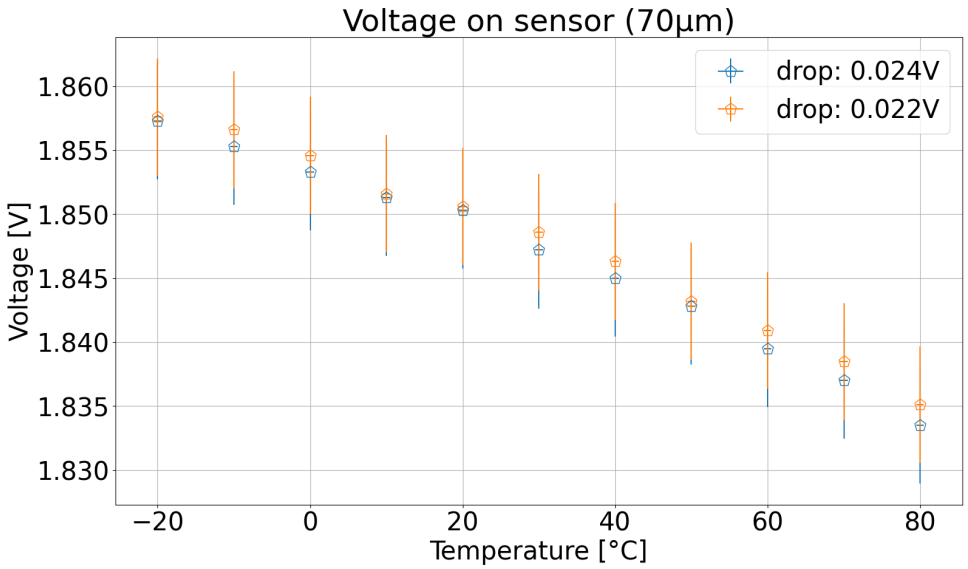

(a) MP11-70-2

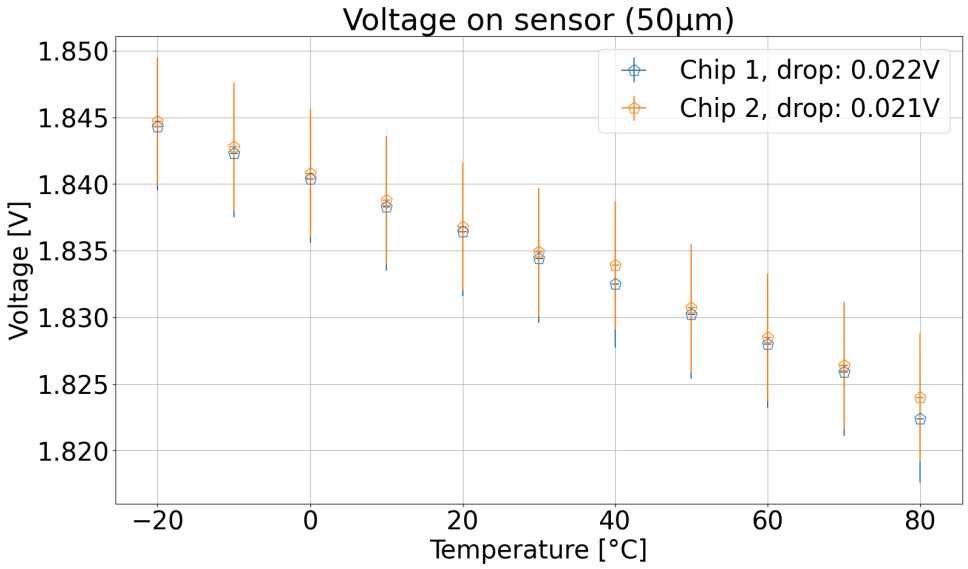

(b) MP11-50

Figure 32: Voltages at two different locations on the chip, VDD1-GND1 (blue) and VDD2-GND2 (orange), with increasing temperature for MP11-70-2 and MP11-50.

10.4. Eye parameters for the MP11-70-2 sensor

The eye parameters as a function of the temperature for the MP11-70-2 sensor are shown in Figure 34. The eye amplitude decrease approximately linear with increasing temperature, from $-20\,°C$ to $80\,°C$ by around $40\,mV$, a drop of 13% from the maximal eye amplitude. This is due to the linear dependence of the resistivity of resistors in the LVDS driver (Figure 18) on the temperature.

The eye height decrease with increasing temperature. This originates on one hand from the linear decrease of the amplitude, on the other hand from the increase of thermal noise with higher temperature. The drop from $-20\,°C$ to $80\,°C$ is about $30\,mV$ or 20%. For temperatures below $10\,°C$ the eye height starts to saturate. One explanation is the increase of noise in the electronics of the sensor for low temperature adding to the thermal noise.

The eye width decreases within the error range linearly over the temperature range, also due to the increase of thermal noise. This decrease by around $12\,ps$ is very small compared to the complete width (around 3%) and does not have a strong influence on the signal quality.

The behavior of the Q-factor resembles the one of the eye height. With rising temperature the Q-factor decreases due to the amplitude drop and the increase in noise with rising temperature. In total the Q-factor drops by around 0.6 (9 %). So the quality of the signal in link 4 mirroring link 1 decreases due to the amplitude drop and the increase in noise, but the eye parameter are

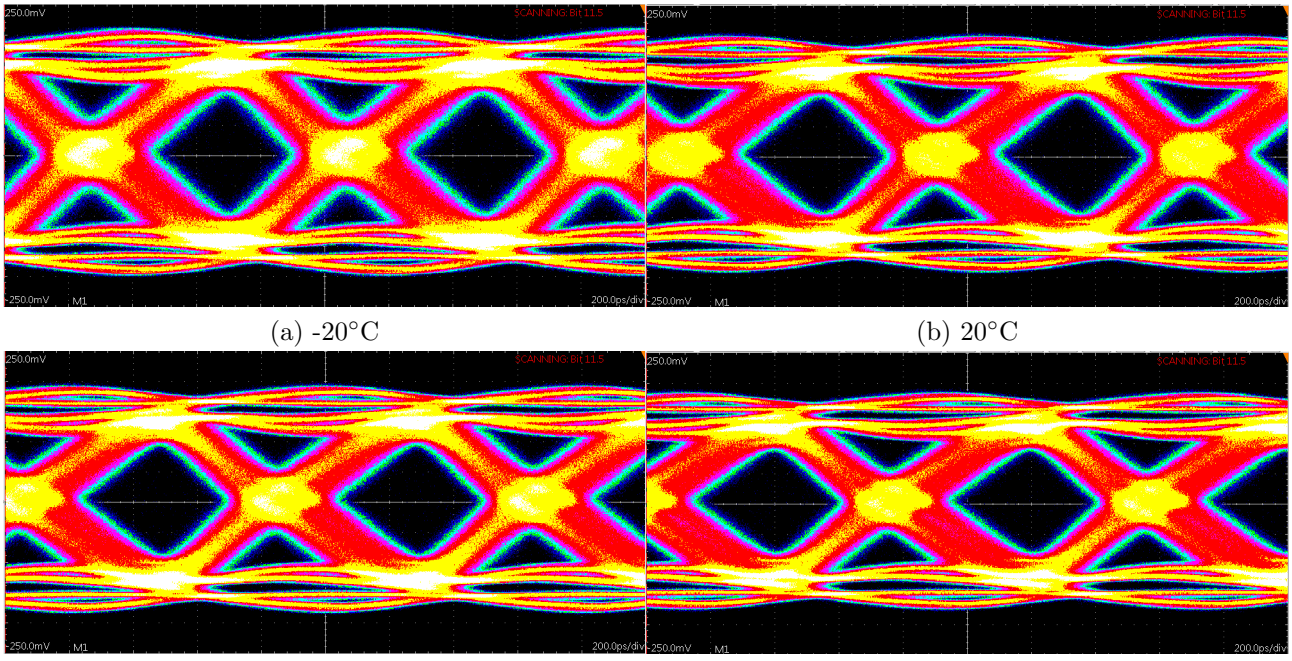

(a) -20°C (b) 20°C

(c) 50°C (d) 80°C

Figure 33: Eye diagram of the MP11-70-2 sensor for different temperatures (measured via link 4 mirroring link 1).

still measurable and no 8/10bit errors occur. Therefore the signal stays stable over the whole temperature range.

10.5. Eye parameters for the MP11-50 sensor

The eye parameter as a function of the temperature for the MP11-50 sensor are shown in Figure 36. The amplitude decreases approximately linear with increasing temperature. As for the MP11-70-2, this is due to the linear dependence of the resistivity of the resistors in the LVDS drivers (Figure 18) on the temperature. The drop in amplitude for this sensor over the whole temperature range is around 60 mV (around 18% of the maximal amplitude).
The eye height decreases with increasing temperature. This originates on one hand from the linear decrease of the amplitude, on the other hand with the increase of thermal noise with higher temperature. The drop from −20 °C to 80 °C is about 65 mV (around 33% of the maximum).
For the temperature range of −20 °C to 0 °C the eye width stays within the error constant due the electric noise getting dominant. For temperatures over 0 °C the width decreases more significant, where the thermal noise is dominant. The eye width overall decreases from −20 °C to 80 °C by about 40 ps (12%). From 20 °C to 30 °C seems to be a jump in the measurement points. It can also be seen in the other eye parameter, indicating a systematic behavior.
Because it is correlated to the noise, the Q-factor evolves with temperature just like the eye height. The overall drop is around 1.3 (17 %), which means a huge decrease in signal quality. Still, the signal stays stable with no 8/10bit errors occuring over the whole temperature range from −20 °C to 80 °C.

10.6. Chip to chip variation

Comparing the influence of temperature on the data link quality of the two sensors MP11-70-1 and MP11-50 one sees qualitatively the same behavior: all eye parameters decrease approximately linear with increasing temperature. The absolute values as well as the strength of the drop differ for the different thicknesses. Looking also on the measurements in section 9 performed with MP11-70-1, one sees for example an eye amplitude of around 315 mV for the standard configuration at room temperature (20 °C). The amplitude at 20 °C for MP11-70-2 is around 275 mV. For the other eye parameters the two 70 µm thick sensors also differ, implying also chip on chip variations for sensors of the same thickness. From these two sensors the variation can be quantify to at least around 40 mV, but to make a real quantitative statement

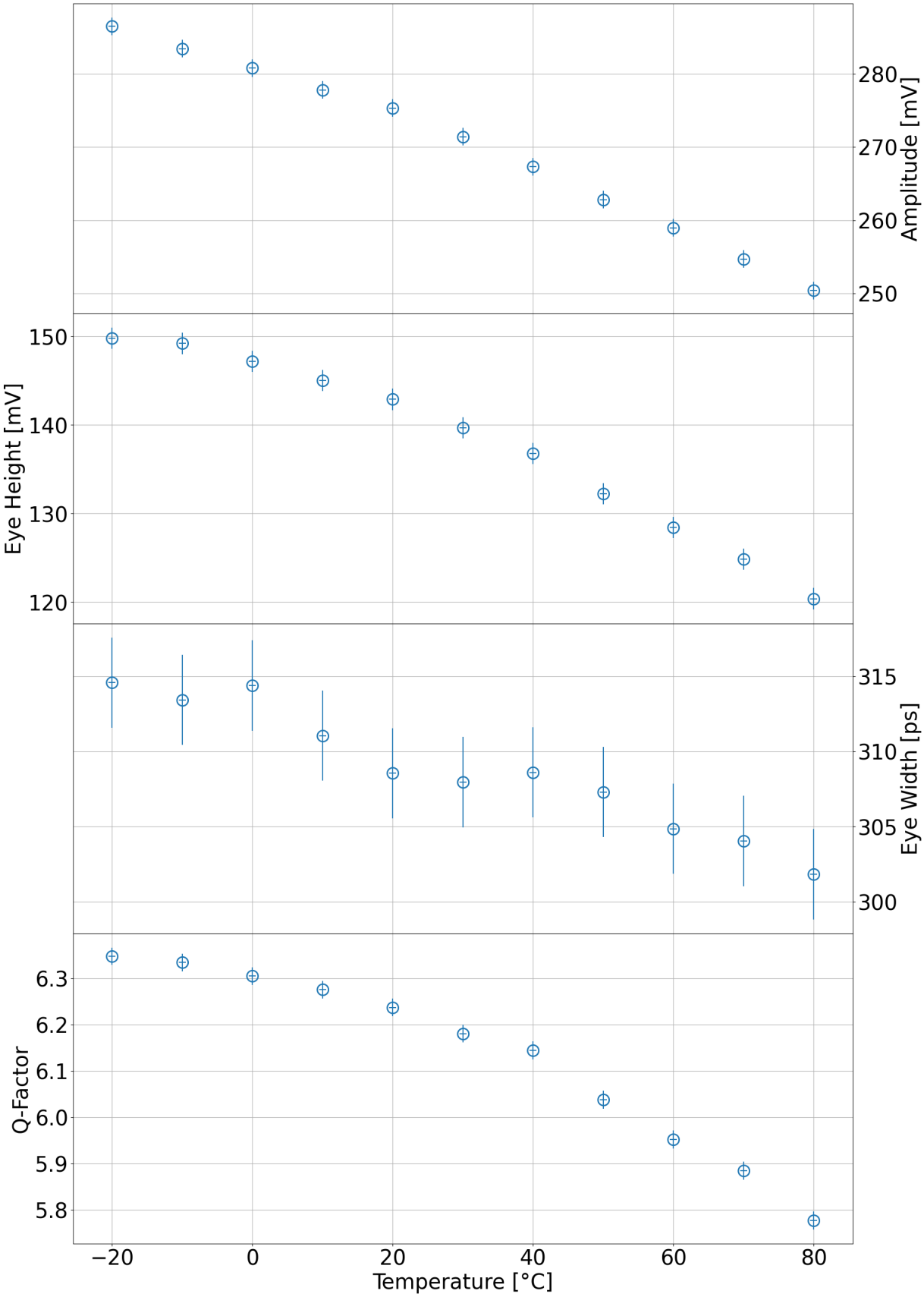

Figure 34: Behavior of the eye parameter for the MP11-70-2 sensor over the temperature range (measured via link 4 mirroring link 1).

two sensors are not enough and a extended study needs to be done. In the quality control of the MuPix11 [32] the chip-to-chip variations are explored in more detail. Qualitatively however the MuPix11 sensors should behave similar for increasing temperature.

10.7. Compensation of the amplitude drop

In subsection 10.4 and subsection 10.5 one can see the amplitude drop and noise increase for increasing temperatures, which is also a major problem for the Q-factor. In this subsection the recovery of the amplitude for high temperatures and increasing the quality of the signal in the data link is qualitatively investigated. The MP11-70-2 is put into an 80 °C environment and the DAC configuration is adjusted. To increase the amplitude the DACs increasing the power in the Dcl serailizer are set to higher values. Figure 37 shows the eye diagrams at 80 °C of the standard configuration and of an adjusted configuration. The adjusted DACs are summed up in Table 6. VPPump has no influence on the power, but still improves the signal quality (see subsection 9.4). Looking at the eye parameter in Table 7, one sees a massive increase of all values for the adjusted configuration. The payoff is an increase of the power consumption by about 93 mW (12 %). In addition the increased power heats the sensor even

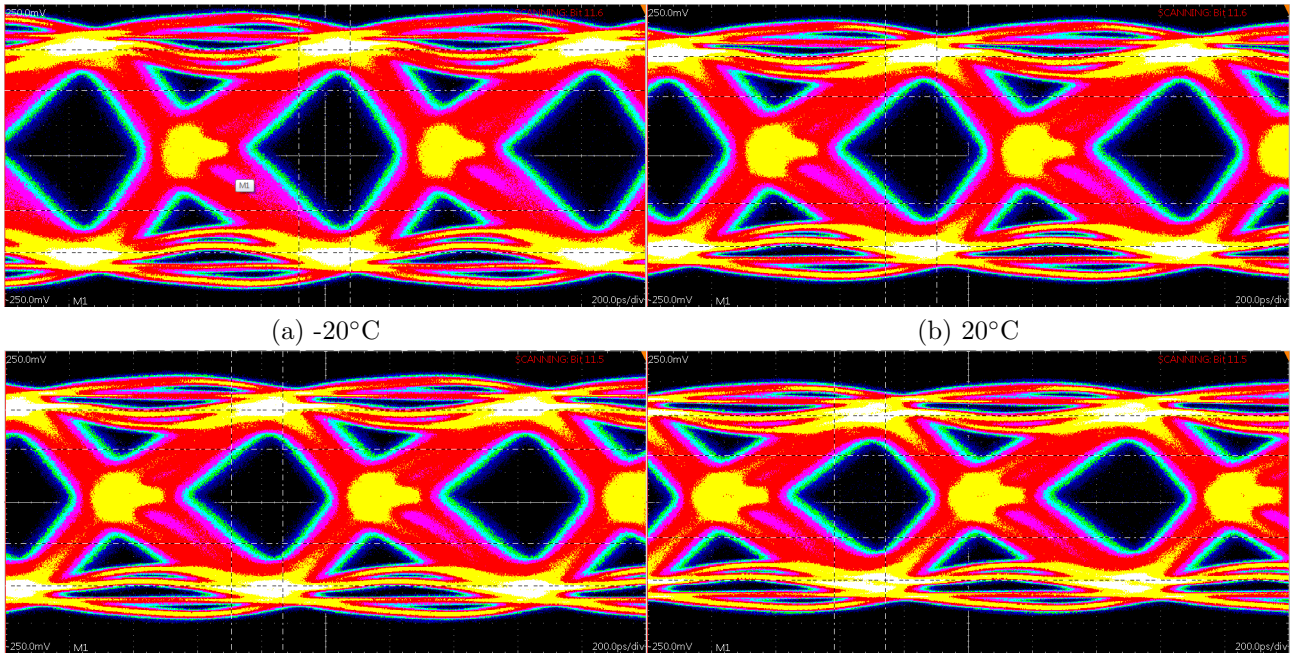

(a) -20°C (b) 20°C

(c) 50°C (d) 80°C

Figure 35: Eye diagram of the MP11-50 sensor for different temperatures (measured via link 4 mirroring link 1).

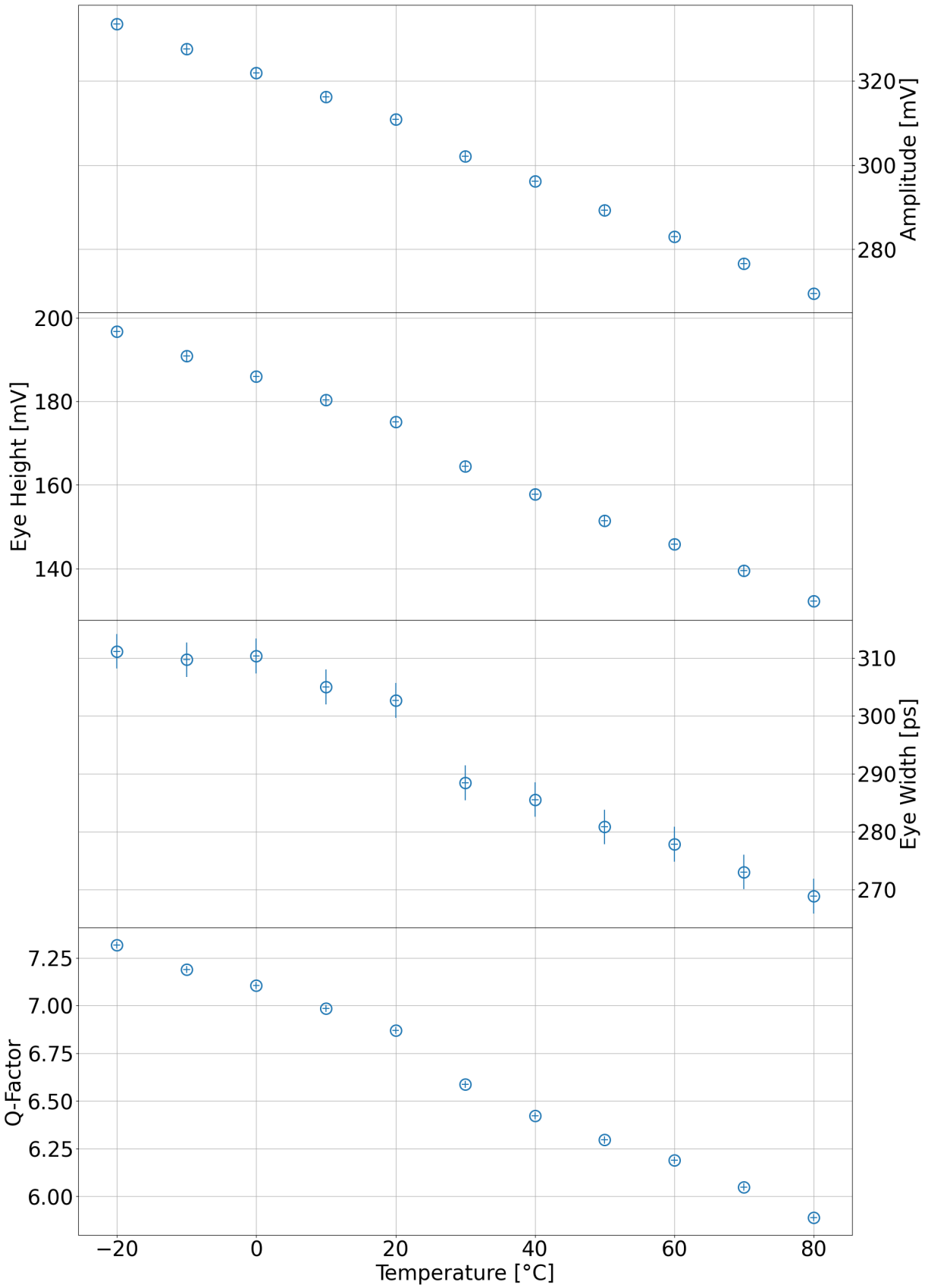

Figure 36: Behavior of the eye parameter for the MP11-50 sensor over the temperature range (measured via link 4 mirroring link 1).

more, decreasing the parameters again. This shows it is possible to compensate the amplitude drop for higher temperatures, but a further optimized and more precise DAC configuration needs to be investigated.

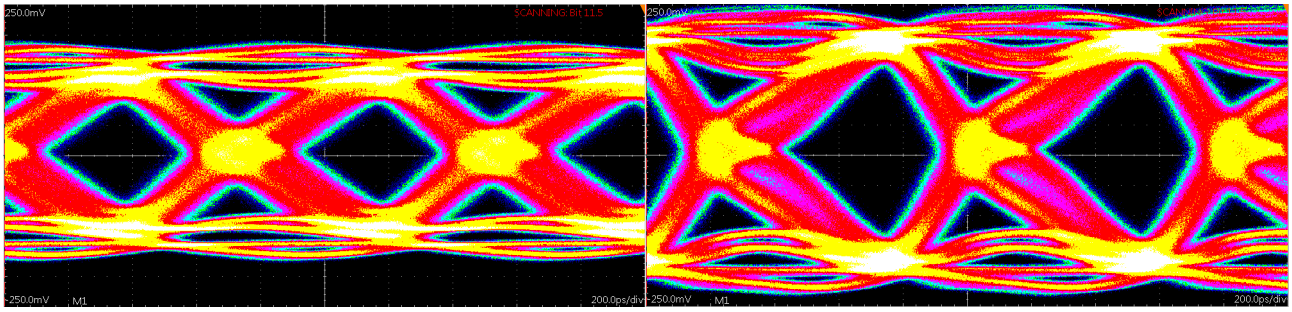

(a) standard configuration (b) adjusted configuration

Figure 37: Compensating of the amplitude drop at 80°C for the 70µm sensor.

DAC	default configuration	adjusted configuration
VPDcl	30	62
VNDcl	15	62
VNLVDS	15	62
VPPump	63	48

Table 6: Default and adjusted configuration to compensate the amplitude drop at 80 °C.

	setting	Amplitude [mV]	Eye Height [mV]	Eye Width [ps]	Q-Factor
20°C	standard	273.874	141.865	301.862	6.22405
80°C	standard	248.854	112.591	268.375	5.47884
80°C	adjusted	350.240	195.313	316.985	6.78204

Table 7: Eye parameter values at 80°C for the standard configuration and an adjusted setting.

11. Data links comparison and mirroring

All measurements of the eye diagrams in section 9 and section 10 were performed over link 4 mirroring link 1. In the Mu3e experiment for the inner layers the data will be acquired from link 1, 2 and 3 directly and in the outer layers from link 4 multiplexing the other three. In this section the different data links are compared as well as the difference of link 4 mirroring other links and multiplexing all of them. MP11-50 is used to perform the measurements.

11.1. Comparison of the different data links

To investigate how link 1, 2 and 3 behave in comparison to link 4 mirroring link 1, all links get rerouted to the SMA connectors on the motherboard (Figure 17). From $-20\,^{\circ}\mathrm{C}$ to $80\,^{\circ}\mathrm{C}$ for each link the eye diagrams are taken in steps of $20\,^{\circ}\mathrm{C}$ and put in Figure 39.
All four data links behave overall very similar and as expected from subsection 10.5: the amplitude and the eye height decreases approximately linear with increasing temperature, the eye width stays roughly constant or decreases by a small degree and the Q-factor decreases approximately linear, except for the Q-factor of link 1. There the values increase from $-20\,^{\circ}\mathrm{C}$ to $80\,^{\circ}\mathrm{C}$ by about 0.2. The improvement of the signal of link 1 originates from the different slopes of the amplitude and eye height drop. While the amplitude decreases with a similar slope as the other links, the eye height of link 1 decreases by the smallest value. The decrease of the eye height and therefore the increase in noise is so small compared to the decrease of the amplitude, the Q-factor defined by Equation 11 increases by around 3%.
The difference in absolute values of the amplitude for the different links originates from the

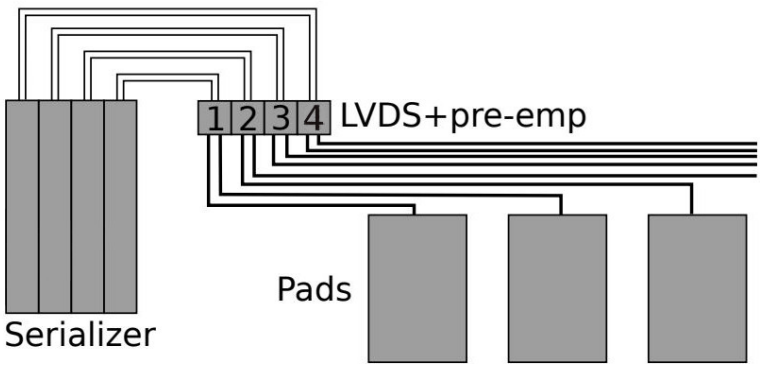

Figure 38: Illustration of connection between the serializer and the pads witin the MuPix11. Adapted from [29].

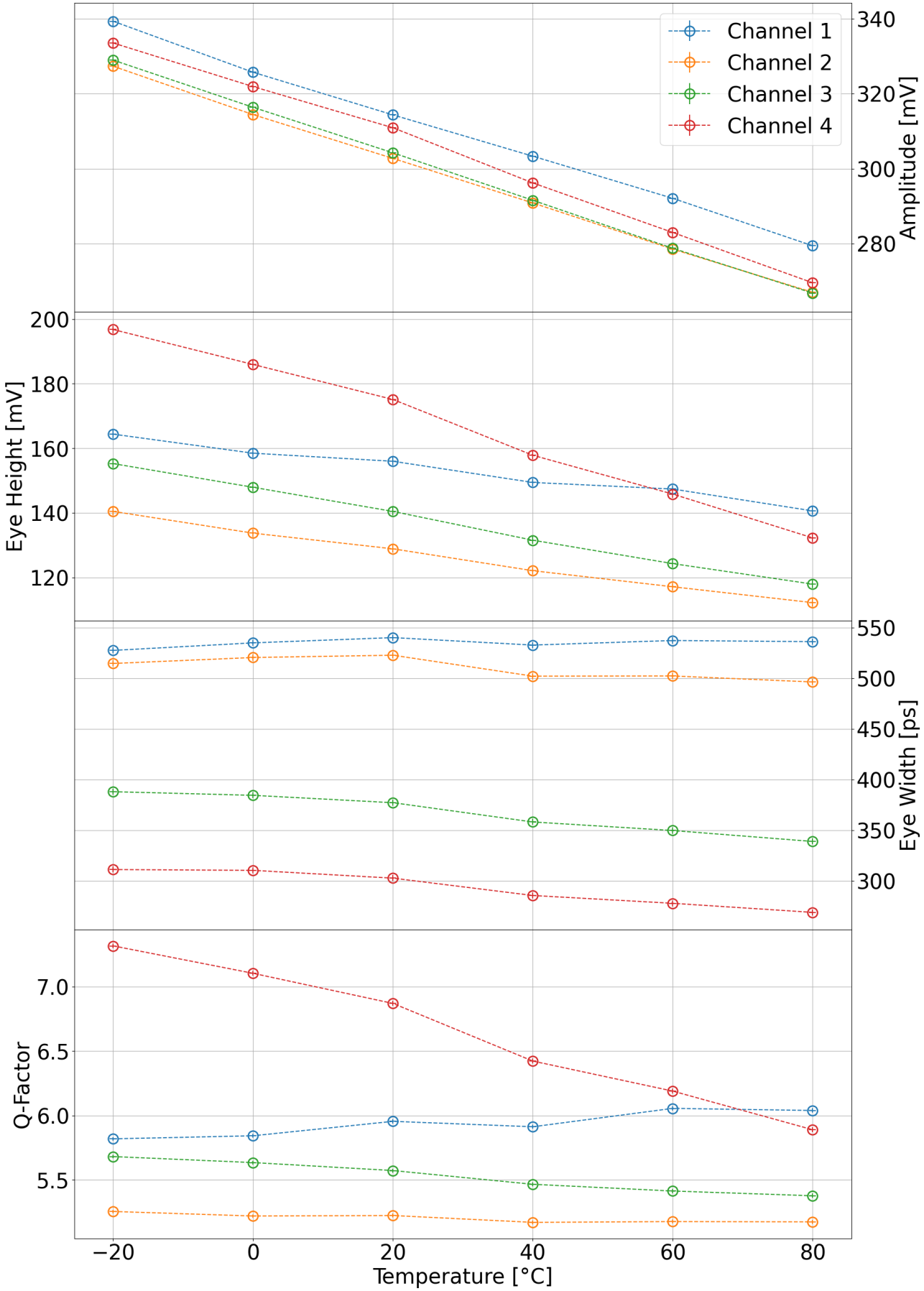

Figure 39: Eye parameter for link 1 (blue), 2 (orange), 3 (green) and 4 mirroring link 1 (red).

setup. The signal goes from the chip to the DSA through different connection lines and components. For example, Figure 38 shows schematically the connections of the LVDS outputs to the pads on the chip, which differ in length for the different links. There alone, different noise effects and amplitude props can occur. Additionally, all connections between the different conducting lines offer opportunities for variations of the data links.

11.2. Different links mirrored and multiplexing

In Figure 40 the eye diagrams and in Table 8 the associated eye parameter values of link 4 mirroring link 1, 2, 3 and multiplexing at room temperature are shown. The eye parameters of mirroring link 1 and mirroring link 3 are equal within the error range. This is expected, since the signal generated on a chip is the same for all matrices.

mirroring	Amplitude [mV]	Eye Height [mV]	Eye Width [ps]	Q-Factor
link 1	272.6 ± 1.2	140.0 ± 1.2	319.6 ± 3	6.17 ± 0.02
link 2	269.3 ± 1.2	129.8 ± 1.2	270.4 ± 3	5.79 ± 0.02
link 3	275.0 ± 1.2	141.8 ± 1.2	307.3 ± 3	6.19 ± 0.02
multiplexing	269.0 ± 1.2	135.5 ± 1.2	310.3 ± 3	6.04 ± 0.02

Table 8: Eye parameter values of link 4 mirroring different links.

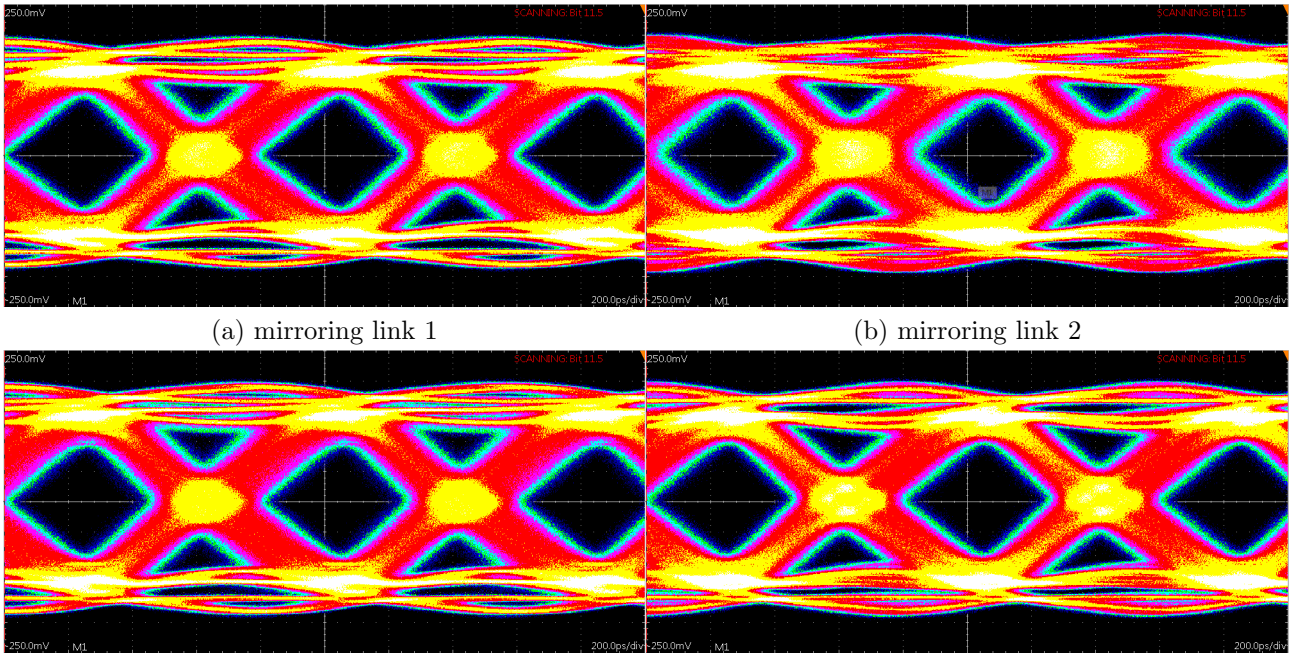

(a) mirroring link 1

(b) mirroring link 2

(c) mirroring link 3

(d) multiplexing

Figure 40: Eye diagram of the different links mirrored and multiplexed by link 4.

A comparison shows a decrease of around 3 mV for mirroring link 2 instead of mirroring link 1. This decrease of less then 1% is not significant and could come from small fluctuations of the power source or of other electrical parts in the system. In contrast the eye height and width drop by roughly 10 mV (7%) and roughly 50 ps (15%), respectively for mirroring link 2 than mirroring link 1. Therefore for mirroring link 2 noise and jitter increase significantly compared to mirroring the other links. Especially the increase in noise, worsens the signal quality, resulting in a drop of the Q-factor by around 0.4 (6%). This could come from some systematic difference in the connection setup of the corresponding lines allowing link 4 to mirroring link 2, considering mirroring the other both links behave the same. Still, the signal quality is with a Q-factor above 5 on a stable level.
To investigate multiplexing, the register DAC "timerend", controling the clock driver to slow down the state machine, is set from 0 to 2. This setting will also be used in the Mu3e experiment. Multiplexing the data streams from link 1, 2 and 3 into one reduces the amplitude by around 3 mV (1%) compared to mirroring link 1, which is no significant drop. The eye height, eye width and Q-factor decrease by around 5 mV (4%), 9 ps (3%) and 0.13 (2%), respectively. Increase in noise and jitter comes from the synchronisation of the three data streams into one, but the signal quality suffers minor loss.
Overall choosing different data links to mirror as well as multiplexing does not influence the signal quality of data link 4.

Part IV.
Discussion

12. Summary

In this thesis, the stability of the data links is investigated. Therefore, the data signal quality of a single sensor setup is observed for different settings of the DACs and for an ambient temperature range from −20 °C to 80 °C.
The investigation of the DAC variation show that the signal quality of the data link is mainly depending on power influencing DACs. VP/VNDelDcl and VP/VNDelDclMux only change the delay and does not affect the signal quality. VN/VPDcl and VNLVDS influence the amplitude and therefore the signal quality. The value for VNDcl can be increased to achieve a higher Q-factor, while the VPDcl is at its highest for the default. VPPump influences the internal clock and therefore the noise and jitter. The signal quality can be improved slightly by setting lower values for the VPPump. Overall the standard configuration of the DAC values are part of an plateau.
To simulate temperature ranges expected in the Mu3e experiment a 70 µm and a 50 µm thick MuPix11 sensor were exposed to an ambient temperature range from −20 °C to 80 °C. The HV current through the sensor diodes increases exponentially with increasing temperature. While the 70 µm thick sensor does not exceed the limit of −100 µA for thermal runaway till 80 °C, the 50 µm thick sensor does at 40 °C for the operation voltage of −15 V. As the chip temperature is about 25 °C higher than the ambient temperature due to self heating, this are already extraordinary high temperatures. The maximum chip temperature of 70 °C, specified by the Mu3e experiment, is therefore already reached at ambient temperatures at around 45 °C. For the 50 µm sensor the voltage can be turned down to −8 V to avoid reaching the limit. Overall, both thicknesses can be safely operated below the temperature and HV current limit.
The power consumption increases with rising ambient temperature by 8 % and 3 % for 70 µm and 50 µm, respectively. The increase originates from the increasing current in the circuitry. The difference for the sensor thicknesses are most-likely due to chip-to-chip variations. The increasing current also leads to a voltage drop on the chips. The drop for both thicknesses is around 1 %. The voltages at 80 °C are at around 1.835 V (70 µm) and 1.825 V (50 µm), still above the minimal supply voltage of 1.8 V for the chip. Overall the sensor operates fully functional in the temperature range at the cost of higher power consumption and higher heat dissipation.
For the investigation of the stability of the data links the Q-factor is used as a measure of the

signal quality. For an increasing ambient temperature from −20 °C to 80 °C a linear decrease in the Q-factor is observed for both thicknesses. The decrease originates from the linear amplitude drop due to the resistivity increase of the circuits resistors and the increase in noise due to thermal noise. The chip-to-chip variations of the sensors decide the strength of the decrease. For the 70 µm and 50 µm sensors the drop over the whole temperature range is 9 % and 17 %, respectively. For the 50 µm sensor a jump in the measurement points at 20 °C is also a reason for the higher drop. Because the jump can be observed in all eye parameters, the effect is most-likely from a systematic problem. Overall, both thicknesses have the same linear decreasing behavior with increasing temperature. Yet a stable operation without transmission errors can be achieved in all cases.
With the knowledge of the influence of the DACs on the eye diagram, the amplitude reduction with increasing temperature can be compensated. By increasing the values of VPDcl, VNDcl and VNLVDS for the 70 µm sensor, the power in the Dcl serializer and therefore the signal amplitude is increased. The VPPump is decreased to reduce jitter. In this way, an increase of the amplitude by around 100 mV, of the eye width by around 38 ps and of the eye height by around 83 mV can be achieved at 80 °C. On the downside a power consumption increase by about 93 mW (12 %) is observed.
The signal for the eye diagrams of the temperature measurement is taken via data link 4 mirroring link 1. To verify a general behavior, link 1, 2 and 3 are observed directly in the temperature range and compared to each other. The behavior of the amplitude, noise and jitter is similar for the data links as to link 4 mirroring link 1. The slight differences observed can come from the different routing of the links and the connection elements. In the single sensor setup only small differences in the amplitudes (1 mV to 15 mV) occur and all links are operational without transmission errors over the whole temperature range.
Comparing the different mirroring modes and the multiplexing of link 4 shows small to none variations. Especially the multiplexing of the data stream, which is important for the outer layers in the Mu3e experiment, has only small losses for the amplitude (1%), eye height (4%), eye width (3%) and Q-factor (2%) compared to mirroring link 1.

The standard configuration of the DACs are all within a plateau, mostly on the left side at low values to reduce power consumption. This allows to increase the DAC values to further stabilize the signal quality if necessary. For an ambient temperature range from −20 °C to 80 °C the sensors can be operated without transmission errors and within the specification of the Mu3e experiment, even without adjusting the DAC settings.

13. Outlook

Overall, the settings used for the single sensor setup are well optimized. The sensor operates without transmission errors in a large range of DAC and temperature variations. However, the measurements are performed with only one or two different sensors, with no handle on chip-to-chip variations. The variations are investigated in the context of the quality control of the MuPix11 [32]. In the future the measurement should be quantified with a higher number of sensors and more measurement points to observe more combination of DAC values and have better quantification of the temperature dependence of chips and their chip-to-chip variation.
In the Mu3e experiment the MuPix11 sensors are not operated as a single sensors, but in ladders and modules. These ladders and modules have different form and data lines, which are realized through so called micro twisted wire pair cables. The measurements of the data links should also be performed with these ladder and module setups to investigate their performance and potential adjust their settings.

Bibliography

[1] Wikipedia contributors. "Standard Model of Elementry Particles". In: *Wikipedia, The Free Encyclopedia* (2024). URL: https://en.wikipedia.org/wiki/Standard_Model.

[2] Ana M. Teixeira. *Lepton flavour violation and neutrino physics: beyond the Standard Model*. 2016. arXiv: 1612.06194.

[3] Douglas Bryman, Shintaro Ito, and Robert Shrock. "Upper limits on branching ratios of the lepton-flavor-violating decays $\tau \to \ell\gamma\gamma$ and $\tau \to \ell X$". In: *Phys. Rev. D* 104 (7 Oct. 2021), p. 075032. DOI: 10.1103/PhysRevD.104.075032. URL: https://link.aps.org/doi/10.1103/PhysRevD.104.075032.

[4] K. Arndt et al. "Technical design of the phase I Mu3e experiment". In: *Nuclear Instruments and Methods in Physics Research Section A: Accelerators, Spectrometers, Detectors and Associated Equipment* 1014 (Oct. 2021), p. 165679. ISSN: 0168-9002. DOI: 10.1016/j.nima.2021.165679. URL: http://dx.doi.org/10.1016/j.nima.2021.165679.

[5] K. Hayasaka et al. "Search for lepton-flavor-violating τ decays into three leptons with 719 million produced $\tau^+\tau^-$ pairs". In: *Physics Letters B* 687.2 (2010), pp. 139–143. ISSN: 0370-2693. DOI: https://doi.org/10.1016/j.physletb.2010.03.037. URL: https://www.sciencedirect.com/science/article/pii/S0370269310003576.

[6] U. Bellgardt et al. "Search for the decay $\mu^+ \to e^+e^-e^+$". In: *Nuclear Physics B* 299 (1988). ISSN: 0550-3213. DOI: https://doi.org/10.1016/0550-3213(88)90462-2. URL: https://www.sciencedirect.com/science/article/pii/0550321388904622.

[7] Marco Ardu and Gianantonio Pezzullo. "Introduction to Charged Lepton Flavor Violation". In: *Universe* 8.6 (May 2022), p. 299. ISSN: 2218-1997. DOI: 10.3390/universe8060299. URL: http://dx.doi.org/10.3390/universe8060299.

[8] P. Roig G. Hernández-Tomé G. López Castro. "Flavor violating leptonic decays of τ and μ leptons in the Standard Model with massive neutrinos". In: *Eur. Phys. J. C (2019) 79:84 Eur. Phys. J. C (2020) 80: 43* (2020). DOI: https://doi.org/10.48550/arXiv.1807.06050. URL: https://arxiv.org/abs/1807.06050v2.

[9] Thomas Theodor Rudzki. "The Mu3e vertex detector - construction, cooling, and first prototype operation". PhD thesis. Ruperto-Carola-University of Heidelberg, 2022.

[10] K. Briggl F. Wauters. *The Mu3e requirements specification book - Chapter 8*. The Mu3e collaboration, 2024.

[11] Norbert Wermes Hermann Kolanoski. *Teilchendetektoren - Grundlagen und Anwendungen*. Springer Spektrum, 2016.

[12] Saverio D'Auria. *Introduction to nuclear and particle physics*. Springer, 2018.

[13] H. A. Bethe J. Ashkin. *Passage of radiation through matter*. 1953.

[14] M. Tanabashi et al. "Review of Particle Physics". In: *Phys. Rev. D* 98 (3 Aug. 2018), p. 030001. DOI: 10.1103/PhysRevD.98.030001. URL: https://link.aps.org/doi/10.1103/PhysRevD.98.030001.

[15] Ali Abd Ali1 et al. "A Comprehensive Study of Conductive Polymer Matrix Composites: A Review". In: *Research Journal of Pharmaceutical Biological and Chemical Sciences* (2017).

[16] Wolfgang Demtröder. *Experimentalphysik 3 - Atome, Moleküle und Festkörper*. 5th ed. Springer Spektrum, 2016. Chap. Halbleiter. URL: https://link.springer.com/book/10.1007/978-3-662-49094-5.

[17] N. David Mermin Neil Ashcroft. *Solid State Physics*. Saunders College Publishing, 1976.

[18] Vančo Litovski. *Lecture Notes in Analog Electronics - Low Voltage Electronic Components*. Springer, 2023. DOI: 10.1007/978-981-19-9868-3.

[19] N. Wermes H. Kolanoski. *Particle Detectors - fundamentals and applications*. Oxford University Press, 2022.

[20] Reza Mirhosseini. "Cross section of two transistors in a CMOS gate, in an N-well CMOS process". In: *Wikipedia, The Free Encyclopedia* (2024). URL: https://en.wikipedia.org/wiki/CMOS#/media/File:Cmos_impurity_profile.PNG.

[21] Jens Kröger. *Characterisation of Silicon Pixel Sensors for High-Energy Physics and beyond*. URL: https://www.physi.uni-heidelberg.de/Einrichtungen/FP/anleitungen/F96.pdf.

[22] Heiko Augustin. "Development of a novel slow control interface and suppression of signal line crosstalk enabling HV-MAPS as sensor technology for Mu3e". PhD thesis. Ruperto-Carola-University of Heidelberg, 2021.

[23] David M. Immig. *MuPix11 - The Mu3e Pixel Tracker Chip*. CLFV2023: The 4th International Conference on Charged Lepton Flavor Violation, 2023.

[24] *DSA8300 Digital Serial Analyzer Printable Application Help*. Tekronix.

[25] *80E00 Electrical Sampling Modules for DSA8300 Datasheet*. Tekronix. 2017.

[26] *Stratix IV Device Handbook, Volume 4: Device Datasheet and Addendum*.

[27] *8b10b Encoder/Decoder MegaCore Function*.

[28] *Anatomy of an Eye Diagram: How to Construct & Trigger*. Tekronix. URL: https://www.tek.com/en/documents/application-note/anatomy-eye-diagram.

[29] Sebastian Dittmeier. "Fast data acquisition for silicon tracking detectors at high rates". PhD thesis. Ruperto-Carola-University of Heidelberg, 2018.

[30] David Maximilian Immig. "Characterization of ATLASPix1, an HV-CMOS Demonstrator for the Phase-II Upgrade of the ATLAS Inner Tracker". MA thesis. Department of Physics and Astronomy, University of Heidelberg, 2019.

[31] Paul Wolf. "On-chip temperature measurements and studies of temperature effects on the pulse shaping of the MuPix11". Bachelor's Thesis. Physikalisches Institut of the University of Heidelberg, 2023.

[32] Anna Lelia Maria Fuchs. "Development of a Quality Control Procedure for MuPix11 Pixel Sensors for the Mu3e Vertex Detector". Bachelor's Thesis. Physikalisches Institut of the University of Heidelberg, 2023.

[33] Ahmed T. A. Mohamed. *Measurement of Higgs Boson Production Cross Sections in the Diphoton Channel with the full ATLAS Run-2 Data and Constraints on Anomalous Higgs Boson Interactions*. Springer Theses, 2020.

[34] B.A. Dobrescu. *Beyond the Standard Model*. Tech. rep. Theoretical Physics Department, Fermilab, Batavia, IL, USA, 2014.

[35] Dhananjay Saikumar. *Exploring the Frontiers: Challenges and Theories Beyond the Standard Model*. 2024. arXiv: 2404.03666.

[36] Sacha Davidson et al. *Charged Lepton Flavor Violation*. 2022. arXiv: 2209.00142.

[37] Rashid M. Djilkibaev and Rostislav V. Konoplich. "Rare muon decay $\mu^+ \to e^+e^-e^+ \nu_e \bar{\nu}_\mu$". In: *Physical Review D* 79.7 (Apr. 2009). ISSN: 1550-2368. DOI: 10.1103/physrevd.79.073004. URL: http://dx.doi.org/10.1103/PhysRevD.79.073004.

[38] Ivan Perić. "A novel monolithic pixelated particle detector implemented in high-voltage CMOS technology". In: *Nuclear Instruments and Methods in Physics Research Section A: Accelerators, Spectrometers, Detectors and Associated Equipment* (2007). DOI: https://doi.org/10.1016/j.nima.2007.07.115. URL: https://www.sciencedirect.com/science/article/pii/S0168900207015914.

[39] *DSA8300 Datasheet*. Tekronix. 2017.

[40] *Fluke 175 Multimeter Datasheet*.

Danksagungen

Mit dieser Seite möchte mich bei den Leuten bedanken, ohne die das alles nicht möglich wär.
Allen voran danke ich Prof. Dr. André Schöning, der es mir ermöglicht hat, Teil einer Arbeitsgruppe zu sein und wissenschaftlich zu arbeiten. Ich möchte das Gelernte und die Erfahrungen während meiner Zeit in der HV-MAPS Gruppe nicht missen.
Vielen Dank auch an Prof. Dr. Norbert Herrmann, der sich als Zweitkorrektor für diese Thesis zur Verfügung gestellt hat.
Ein herzlichen Dank geht an Dr. Heiko Augustin, der mich vom Anfang an unterstützt hat und stets eine Antwort auf meine Fragen hatte.
Vielen Dank an Ruben Kolb, David Immig, Benjamin Weinländer, Sebastian Dittmeier, Dr. Tamasi Kar und Lukas Mandok für das Lesen meiner Thesis und euren wertvollen Input.
Schließlich möchte ich mich herzlich bei meiner Familie bedanken, ohne deren Unterstützung ich niemals so weit gekommen wäre. Auch in schwierigen Zeiten war es immer schön zu wissen, dass ich auf sie zählen kann.

Erklärung

Ich versichere, dass ich diese Arbeit selbstständig verfasst und keine anderen als die angegebenen Quellen und Hilfsmittel benutzt habe.

Heidelberg, den 10.07.2024,

Florian Schlötzer